

Structure-Dynamics Relationships in Complex Fluids and Disordered Porous Solids Assessed using NMR

Von der Fakultät für Physik und Geowissenschaften

der Universität Leipzig

genehmigte

D I S S E R T A T I O N

zur Erlangung des Akademischen Grades

Doktor rerum naturalium

Dr. rer. nat.

vorgelegt

von Dipl.-Phys. Alexander Shakhov
geboren am 16. März 1986 in Fatezh

Gutachtern:

PD Dr. Rustem Valiullin

Prof. Dr. Ernst Röbler

Tag der Verleihung: 22.09.2014

Abstract

Shakhov, Alexander

Structure-Dynamics Relationships in Complex Fluids and Disordered Porous Solids Assessed using NMR

Leipzig University, Dissertation, 2014

101 pages, 86 references, 4 tables, 59 figures

A NMR study of the structure-dynamics relationships in heterogeneous materials is presented. In the first part, transport in soft-matter systems is studied using the pulsed field gradient NMR technique (PFG NMR). The molecular crowding effect in biological matter has been addressed using polymer solutions as model systems. By performing ensemble-based diffusion studies, the earlier obtained data on anomalous diffusion have been complemented. The transition to normal diffusion on a larger time scale has been shown. Taking advantages of the NMR approach, transport properties of microemulsions consisting of micellar colloids dissolved in liquid crystals have been investigated. The self-diffusivities measured under equilibrium conditions have shown weak correlations with microscopic ordering and macroscopic phase transitions occurring in the systems under study. The formation of micelles is shown to be decisive for macroscopic separation at the isotropic-nematic transition.

The second part of the thesis covers heterogeneous effects in diffusion for fluids in porous solids, as probed using a combination of NMR diffusometry and structure characterization methods. Ionic liquids have been investigated, revealing a complex behavior under confinement. The attempts to correlate the observed characteristics of the ionic liquids with their internal chemical structure were undertaken. Finally, the series of nanoporous glasses with tunable pore structure characteristics were studied. Strong correlations between their structure and the preparation conditions as well as between the resulting transport properties have been shown.

Contents

1	Introduction	1
2	Basics of Diffusion and Experimental Techniques	5
2.1	Fundamentals of Diffusion	5
2.2	PFG NMR	8
2.3	NMR Cryoporometry	13
3	NMR in Heterogeneous Systems	19
3.1	Diffusion in Crowded Media	19
3.1.1	Anomalous Diffusion in Dextran Solutions	19
3.1.2	Experiments and Discussion	22
3.2	Investigation of Complex Fluids	29
3.2.1	Nematic Microemulsions	29
3.2.2	Diffusion in Liquid-Crystal Microemulsion.	35
3.3	Ionic Liquids under Confinement	48
3.3.1	Ionic Liquids and Confinement Medium	48
3.3.2	Melting of Ionic Liquids	55
3.3.3	NMR Cryoporometry using Ionic Liquids	58
3.3.4	Diffusion of Ionic Liquids	62
3.3.5	Correlations between the Structure and Properties of Ionic Liquids	66
3.4	Diffusion in Nanoporous Glasses	68
3.4.1	Porous Glasses Obtained by Spinodal Decomposition	68
3.4.2	Nitrogen Adsorption Data	70
3.4.3	Results of NMR Cryoporometry Experiments	73
3.4.4	Diffusion Study	78
3.4.5	Conclusions	82
4	Summary	85
	Bibliography	89
	Acknowledgements	97

List of Publications	99
Curriculum Vitae	101

Chapter 1

Introduction

The phenomenon of diffusion is a cornerstone of multiple processes occurring in nature. Its first quantitative description was given by Adolf Fick, who published his results in Leipzig, 1855 [1]. Although the basic laws of diffusion in a variety of physical systems have already been understood, this topic still attracts a substantial attention. Nowadays, the focus in this research area is shifted to more complex systems in which spatio-temporal variations of relevant physical quantities on microscopic scale, e.g. diffusion mechanisms, may give rise to quite complex macroscopic transport phenomena. As an exemplification of such situations, one may refer to systems with dominating interactions on nanoscale resulting in structural self-organization of matter. These effects may have quite different physical origin, such as surface interactions in nanoporous materials, hydrophilic/hydrophobic interactions in surfactant mixtures, dynamical constraints in polymer systems, etc. In turn, the occurrence of mesoscopically ordered phases may strongly affect the rates of molecular propagation in these systems. Exactly this topic of current sciences, namely establishing the structure-dynamics relationships in heterogeneous materials, was in the focus of this study.

Nowadays, there exist a large variety of experimental techniques used for the investigation of translational dynamics. One may refer, among others, to dynamic light scattering, macroscopic permeation methods, fluorescence correlation spectroscopy (FCS) and single particle tracking (SPT). In our work, we have used pulsed field gradient NMR (PFG NMR) as the most suitable technique. It is non-invasive and non-perturbative, i.e. the molecular systems can be studied without introducing any external interference [2]. Notably, it can easily be combined with other experimental methods of structural characterization. In this way, structure-dynamics

relationships can be addressed in the most direct way. The new knowledge obtained may, in turn, give rise to the development and the optimization of already existing methods for material characterization as well as to the option to improve the material characteristics.

In this work, the advantages of PFG NMR were utilized to study the structure-dynamics relationships for several systems:

(1) Nanoporous materials are organic or inorganic frameworks, containing pores with sizes less than 100 nm [3]. In our work, we studied nanoporous solids, obtained by leaching of phase-separated alkali borosilicate glasses [4], which have attracted a lot of attention in the field of catalysis, mass separation, drug delivery, etc. This interest originates from their favorable characteristics, such as a very large internal surface area and, more importantly, due to the ability to tune porosity and the character of the pore interconnectivity. The conventional method for structural characterization and determining of above-mentioned parameters is the adsorption technique. We have shown that PFG NMR in combination with NMR cryoporometry applied to the considered glasses can yield some additional information about structure, including their diffusion properties. Establishing structure-dynamics relationships allowed us to conclude about possible ways of optimization of the properties of nanoporous glasses, which, in turn, can be accomplished by varying the preparation conditions.

(2) Ionic liquids (IL) are salts in liquid state made of ions and short-lived ion pairs [5]. They are found to be very promising electrolytes [6]. Therefore, deeper understanding of transport properties of IL is potentially important for practical applications in energy industry. The confinement imposed by a porous matrix is expected to have an effect on ionic liquids. They possess an additional parameter, namely the electric charge, which, in turn, can lead to additional effects. Ionic liquids adsorbed in disordered porous glasses have, indeed, shown [7] a very low melting temperature in comparison to the bulk state. Using several porous glasses as a medium for confinement and several ionic liquids as probes, we have tried to obtain deeper insight into their behavior. A detailed characterization of porous glasses has been performed by using NMR cryoporometry, together with nitrogen adsorption. On the basis of these data, a model rationalizing the dynamic behavior of ionic liquids under confinement was suggested, which attempts to correlate the observed characteristics of the ionic liquids with their internal chemical structure and the confining medium.

(3) Another interesting class of problems considered in this work are heterogeneous systems, in which confinement effects are exerted on more bulky molecules, namely on polymers of high molecular weight. Such systems proved to be a good model system to simulate the diffusion dynamics in ordinary living cells [8]. A cell, generally speaking, consists of a mixture of bio-polymers dissolved in a liquid phase. Diffusion driven mechanisms play a crucial role in the internal chemistry of the cell. Since diffusion measurements *in vivo* are not easily accessible, model systems consisting of different polymers dissolved in water, were usually applied to mimic bio-objects for the *in-vitro* explorations. However, the investigation of such prepared solutions raised a number of controversies [9], especially related to the description of an effect referred to as molecular crowding. This phenomenon takes place in a concentrated polymer solution, which is similar to the living cell. Branched glucan (dextran) was chosen, in several studies, as a model polymer. In such kind of systems, investigated mostly by fluorescence correlation spectroscopy (FCS) technique, deviation from normal diffusion has been observed. The fundamental mechanisms governing such anomalous behavior, however, remained essentially unrevealed. We have used the potentials of PFG NMR to separately record the propagations patterns of the individual components in composed systems for tracing the time and length scales of ordinary diffusion. We succeeded in reducing the gap between both techniques, leaving a very narrow range of molecular length paths, where the transition from anomalous (at shorter length scales) to normal diffusion (at longer ones) must be expected to occur.

(4) The advantages of NMR were further exploited by investigating another example of complex heterogeneous system, namely nematic microemulsions (NM). They consist of nano-sized micelles dissolved in a liquid crystal. It has been shown that such microemulsions possess a local order making, which has been referred to as a new phase of matter [10]. However, the initially proposed description of phase transformations has been questioned in subsequent works [11, 12]. In addition, the mechanisms of phase separation and their physical nature remained unresolved [13]. Since the microemulsion considered in the study is highly dynamic and sensitive to temperature variations, NMR proved to be a suitable technique for investigating this system, allowing a precise control of the relevant structural and dynamic parameters. To the best of our knowledge, we have performed the first direct diffusion measurements of all components composing the system. As a result, the dynamics of phase transformations could be rationalized on the basis of the observed diffusion behavior.

Chapter 2

Basics of Diffusion and Experimental Techniques

2.1 Fundamentals of Diffusion

Diffusion (lat. spreading, scattering) is one of fundamental transport phenomena that occur in nature. The concept of diffusion is applicable in many areas of natural sciences such as physics, chemistry, biology, etc. and also may be applied to socioeconomic processes like demography or financial markets. From the atomistic point of view, diffusion is considered as a result of the random walk of the diffusing particles, which are self-propelled by thermal energy. The first direct observation of random walk was accomplished in 1827 by Robert Brown who noticed that grains of pollen suspended in solution undergo a continuous motion. Obviously, the experimental technique at that time did not allow to access the atoms and to reveal the underlying mechanisms of this remarkable phenomenon. The first, non-atomistic approach to diffusion was developed by Adolf Fick. He described it as a flux which is proportional to the negative gradient of concentrations. It goes from regions of higher concentration to lower ones, with a magnitude that is proportional to the concentration gradient:

$$J = -D \frac{dc}{dx} \quad (2.1)$$

where J is the "diffusion flux" (amount of substance per unit area per unit time). J measures the amount of substance that will flow through a small area during a small time interval. D is the diffusion coefficient or diffusivity, c is a concentration, x is the position.

Mass conservation gives the second Fick's law that predicts how diffusion causes the concentration to change with time:

$$\frac{dc}{dt} = D \frac{d^2c}{dx^2} \quad (2.2)$$

The theory of Brownian motion and its atomistic background were developed by Albert Einstein in 1905. He related the mean square displacement (MSD) of an ensemble of randomly moving particles to their self-diffusivity D :

$$\langle r^2(t) \rangle = 6Dt \quad (2.3)$$

where t is the diffusion time. The mean square displacement can be related to the so-called probability density function (PDF), which gives the likelihood to find a randomly moving particle at some distance x from its starting position at a time t . The function, called propagator, plays the crucial role in PFG NMR as it will be shown later. More generally, the MSD obeys a power law:

$$\langle r^2(t) \rangle = 6D_{eff}t^\alpha \quad (2.4)$$

where the parameter D , appearing in this equation, becomes an "effective" diffusivity, defined by the relation:

$$D_{eff} = \langle r^2(t) \rangle / 6t \quad (2.5)$$

as the ratio between the MSD and (6 times) the observation time. For normal diffusion the thus defined parameter is clearly seen to coincide with the self-diffusivity. For anomalous diffusion, however, the diffusivities recorded in PFG NMR measurements are seen to follow the relation:

$$D_{eff} \propto t^{-(1-\alpha)} \quad (2.6)$$

If $\alpha < 1$ the system undergoes so-called anomalous subdiffusion, if $\alpha > 1$ - superdiffusion. The corresponding mean square displacements are shown in Figure 2.1. The anomalous superdiffusion arises in mathematical applications related to chaos theory and can be also used in stochastic measurement and simulations for multiple phenomena like earthquakes, signal analysis, financial mathematics, cryptography as well as for applications in physics. Multiple examples of anomalous subdiffusion, in turn, were found in biological systems.

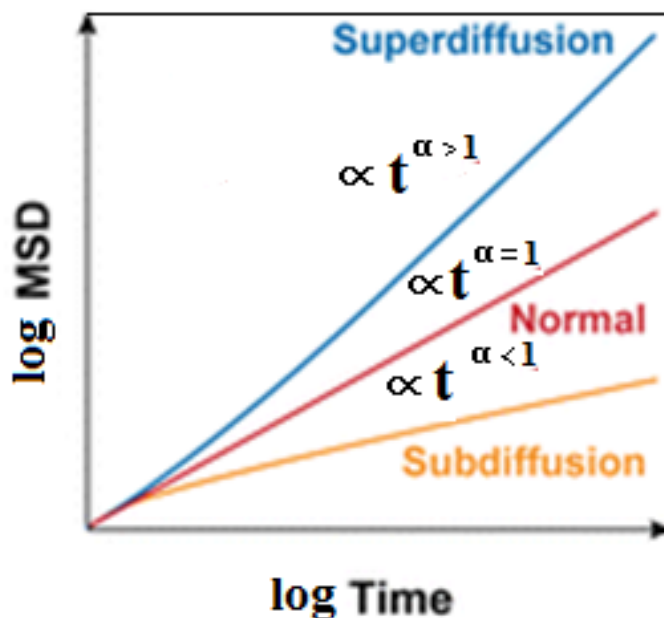


FIGURE 2.1: Mean square displacement in case of normal, anomalous sub- and superdiffusion.

Considering the classical Brownian experiment with grains of pollen, Einstein used an atomistic approach with Stokes law for spherical particles moving in a viscous liquid in the limit of low Reynolds numbers and has obtained the famous Stokes-Einstein equation:

$$D = \frac{kT}{6\pi\eta R} \quad (2.7)$$

where k is the Boltzmann constant, T is the temperature, η is the viscosity of the liquid and R is the radius of the diffusing particle.

Since the diffusivity depends on temperature, which is one of the major factor ruling chemical kinetics, one may often consider the connection between diffusion coefficients and reactions rates occurring in chemical compositions as well as in biological systems. Therefore, knowing only D , one may describe and analyze a multitude of processes which are taking place in nature. Thus, the accurate measurement of the diffusion coefficient is a matter of high interest in experimental science.

2.2 PFG NMR

Since its discovery, nuclear magnetic resonance has become a widely-used tool for the investigation and the characterization of a large variety of materials. It allows probing the transport of liquids and gases in multiple physical systems non-invasively. Moreover, one may change parameters of the sample under investigation like temperature, pressure, loading, etc. and measure its dynamical characteristics simultaneously. NMR technique operates with the system of spins placed in a magnetic field. There are several atoms suitable for NMR spectroscopy like 1H , 2H , ^{19}F , ^{13}C . Since hydrogen is abundant in nature and present in every organic compound, 1H NMR spectroscopy is used predominantly. In our work, we mainly use one particular NMR technique, namely pulsed field gradient (PFG) NMR. One may decompose the standard PFG NMR measurement procedure into several steps [14]:

a) Alignment of a system of nuclear spins along a strong magnetic field (in our case with $B = 9.4$ Tesla), where the spins perform a precessing rotation with the so-called Larmor frequency:

$$\omega = \gamma B_0 \quad (2.8)$$

where γ is the gyromagnetic ratio for the nuclei used.

b) The perturbation of spins with an electromagnetic, usually radio frequency (RF) pulse, to create an initial spin coherence.

c) The application of an additional gradient along the magnetic field (axis z). Thus the Larmor frequency of spins becomes spatially spreaded:

$$\omega = \gamma(B_0 + gz) \quad (2.9)$$

where g is a gradient.

The gradient is applied during a certain time interval δ , during which the spins acquire a phase shift:

$$\varphi = \gamma g z \delta \quad (2.10)$$

This procedure is called "encoding".

d) Given the system some time to evolve, a second gradient is applied. It causes a phase shift in the opposite direction, thus the phase acquired during the encoding period is compensated by this second gradient pulse ("decoding").

However, for diffusing species, this re-phasing can be incomplete and a phase difference remains. This happens because the diffusing spins change their positions in space and henceforth their Larmor frequencies. The compensation is complete for the nuclei, which do not move, i.e. do not change their Larmor frequencies during the whole experiment. It may be shown that the attenuation $S(q,t)/S(0,t)$ of an original spin-echo signal due to molecular diffusion is the Fourier transform of the so-called mean propagator $P(z,t)$:

$$S(q,t)/S(0,t) = \int P(z,t)e^{iqz} dz \quad (2.11)$$

which was mentioned in the previous part. Here $q = \delta\gamma g$ is so-called scattering wave number, $S(0,t)$ is the signal intensity in the absence of magnetic field gradients. The propagator $P(z,t)$ gives the mean value of probability, that during time t a molecule will be shifted over a distance z .

Since the solution of Fick's second law gives the expression for propagator in case of one-dimensional diffusion as:

$$P(z,t) = \frac{1}{\sqrt{4\pi Dt}} \exp\left(-\frac{z^2}{4Dt}\right) \quad (2.12)$$

one can readily obtain the spin-echo attenuation in an exponential form:

$$S(q,t)/S(q,0) = \exp(-q^2 Dt) \quad (2.13)$$

Thus, the diffusivity may be easily determined from the slope of semi-logarithmic intensity versus $q^2 t$.

Our laboratory is equipped with two spectrometers operating at 400 MHz and 125 MHz proton resonance frequency. They have a home-built PFG unit, allowing the application of magnetic field gradient pulses with amplitudes up to 35 T/m with very short rise and fall times. Materials under study are loaded into glass tubes with diameter 0.8 mm. The procedure of sample preparation (porous materials) often involves the activation, i.e. the heating up to high temperatures with subsequent pumping to remove possible impurities like water, undesired air, etc.

Since the NMR is quantitative, the signal measured is directly proportional to the number of spins. However, the loading of the sample can be changed upon the measurement. It can be done by connecting the probe to the gas phase with consequent changing of pressure.

The measurements are accessible in a broad range of temperatures between -120 °C (see the next part about NMR cryoporometry) and up to $+120$ °C.

We used a home-written script to control all parameters of the experiments. The choice of the applied pulse sequences is dictated by properties of materials under study and by data desired to obtain. To introduce the language of PFG NMR and parameters tuned during the experiment, the example of one simple sequence, namely Hahn spin echo with pulsed field gradients, is given in Figure 2.2.

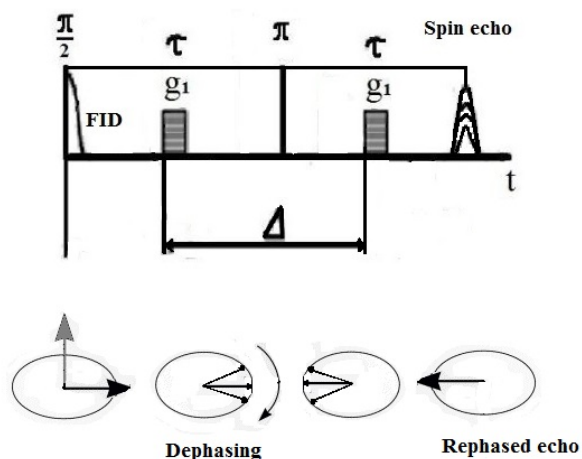


FIGURE 2.2: Hahn gradient pulse sequence for PFG NMR experiment.

This working principle of this sequence can be explained as follows:

- a) $\frac{\pi}{2}$ radio frequency pulse (P90) brings the system of spins in resonance, that means the spins are rotated into the plane XY, which is perpendicular to the direction of magnetic field (axis z). Consequently, NMR signal is detected. Its duration is limited by the spin-spin relaxation, also called T_2 -relaxation. The NMR signal thus obtained is called free induction decay (FID). In liquids it has the duration up to several seconds. However, in adsorbed or high molecular systems it may be much shorter.
- b) The first magnetic field gradient pulse encodes the system of spins, i.e. gives rise to the linear dependence to Larmor frequency of the spins along the magnetic field as it was described before (Eq. 2.9).
- c) The spin-spin relaxation as well as external magnetic field inhomogeneities force different spins in the sample to precess at different frequencies that, in turn, leads

to the loss of the net magnetization. The inhomogeneous part of the magnetization loss of the NMR signal can be removed by applying a π (P180) inversion pulse. As a result, the system of spins is refocused again.

d) Finally, after using the second gradient pulse, which decodes the system of spins, the NMR signal is formed and measured.

By repeating the measurements with different magnitudes of the gradient pulses, the diffusion is assessed on the basis of Eq. 2.11.

For diffusion studies, the stimulated echo pulse sequence as well as 13-interval pulse sequence with bipolar gradients has been used. Some unwanted phenomena during the experiments may prevent the determination of the genuine diffusion coefficients. One of such sources is the occurrence of the internal magnetic field gradients in porous materials induced due to different magnetic susceptibilities of the solid matrix and porous spaces containing guest molecules in the gaseous or liquid phases. Another problem is encountered due to the presence of eddy currents, which appear during switching on and off of the magnetic field gradients during the PFG NMR experiments. The 13-interval sequence is proved to be an appropriate sequence to reduce these negative effects. The schematics of the 13-interval pulse sequence with bipolar gradients and corresponding P90 and P180 RF pulses are shown in Figure 2.3.

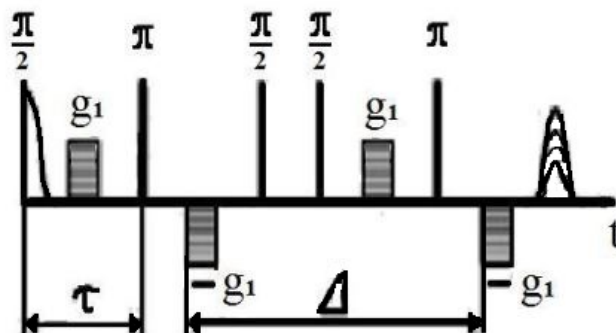


FIGURE 2.3: 13-interval pulse sequence for PFG NMR experiment.

In this paragraph, we give some typical parameters used in our experiments. The durations of the P90 and P180 pulses was mostly in the range 5-15 μs and 10-30 μs , respectively. The diffusion time was varied between 8 ms up to several seconds. Other important parameters, such as relaxation delay (RD), receiver gate (RG), maximal gradient amplitude, gradients durations, etc. were selected depending on the sample properties. The typical diffusion experiment lasted between several

minutes up to several days in the case of low signal-to-noise ratio in order to increase the accuracy of the measurements.

For the PFG NMR experiments, the 13-interval pulse sequence incorporating magnetic field gradient pulses was used [15]. The time interval τ between the 90 °C and 180 °C pulses was typically kept to 1 ms, the diffusion time t_d was varied between 10 and 200 ms. With the latter, by proving that the diffusion attenuation functions measured did not depend on t_d , it was ensured that the genuine intra-particle diffusivities (not retarded by the unwanted boundary effects) were measured. To access the diffusivities under different loadings by a test liquid, the NMR samples with the porous materials were connected to a big reservoir, in which vapor of the liquid could be prepared at a required pressure [16]. By bringing the material into contact with the reservoir and giving a sufficient time to equilibrate, well-defined amounts adsorbed θ were prepared. In this way, both θ and the diffusivities were probed under identical thermodynamic conditions. Therefore, cyclohexane, which has a relatively high saturated vapor pressure allowing an accurate control of the pore loadings, was used as a probe liquid for the diffusion measurements. The measurements were performed on both adsorption, i.e. upon pressure increase, and desorption, i.e. upon pressure decrease [17].

2.3 NMR Cryoporometry

NMR cryoporometry was introduced by Strange et al. [18]. It has become a powerful method for structured characterization of porous materials with complex pore morphologies [19, 20]. The technique is based on the Gibbs–Thomson effect: small crystals, which one finds upon freezing of liquids in pore spaces, melt at a lower temperature than infinitely large crystals. This temperature shift is defined by the well-known Gibbs–Thompson equation:

$$\Delta T_m(x) = \frac{k}{d_c} \quad (2.14)$$

where k is a material-related constant, which depends on the bulk melting point of the liquid used, d_c is a size of the solid frozen core, which is given as the difference between the pore diameter and the thickness of an unfrozen layer.

The primary goal of NMR cryoporometry is to find the pore size distribution (PSD) for a given porous sample.

NMR cryoporometry relies on a large difference in the transverse NMR relaxation rates between solid and liquid phases. By choosing an appropriate inter-pulse delay τ in the spin-echo pulse sequence, the NMR signal intensity I solely from the liquid phase can be measured. The thus measured signal reflects the relative fraction of the pores filled by the liquid at a given temperature. Based on equation (2.14), one can derive equation (2.15) which gives the PSD for the material under study:

$$\frac{dI}{dx} = \frac{dI}{dT_m(x)} \frac{dT_m(x)}{dx} = \frac{dIk}{dT_m(x)x^2} \quad (2.15)$$

where $\frac{dI}{dx}$ is the relative volume of pores with a size x . The typical result of NMR cryoporometry experiment is presented in Figure 2.4.

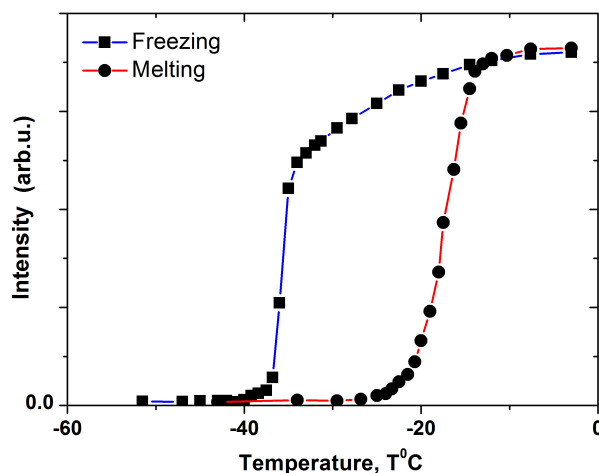


FIGURE 2.4: Freezing and melting curves obtained during an NMR cryoporometry experiment for a mesoporous sample filled with water.

It shows the evolution of the system upon cooling below 0 °C, which is the equilibrium transition temperature for bulk water. It is important to mention that samples prepared for our studies always had a bulk liquid phase surrounding the monolithic particles with the inner pores. During the first step of NMR cryoporometry measurements, the samples are cooled till the NMR signal disappears, i.e. the liquid freezes completely. Then, the temperature is increased almost to 0 °C. At this temperature the bulk phase is still frozen, while the liquid in pores is found in the molten (liquid) state. After that, the NMR signal intensity is measured upon cooling and subsequent heating. The thus measured curves are referred to as freezing-melting curves. The role of the frozen bulk phase will be explained below. Similarly to the gas adsorption methods, the hysteresis between freezing and melting is often observed. The occurrence of hysteresis is associated with the existence of metastable states, which may be encountered during both freezing and melting. The mechanisms giving rise to the freezing-melting hysteresis in porous systems are still a matter of active discussions. A brief description of these mechanisms is given further.

Let us start with the freezing behavior. According to the Gibbs-Thompson equation, the system has to be cooled to achieve the temperature, when liquid in pores freezes. In general, this freezing could proceed via two scenarios. The first one is related to the existence of the barriers in the free energy for homogeneous nucleation. In this case, the system must be cooled even much below the temperature predicted by the Gibbs-Thompson equation. This scenario, however, is avoided in our experiments, because of the direct contact to the frozen bulk phase, which

plays a role of the nuclei of the crystal phase in pores. Therefore, liquid in the pores can be frozen solely via propagation of the freezing front from the outer surface of the porous particle, i.e. from the pore openings, towards its center.

The real situation is more complex. In our experiments, the systems of interconnected pores were investigated. In this case, one may imagine a geometrical situation sketched in Figure 2.5a, showing that larger pores do not have a direct access to the outer frozen phase, but connected to the external gas reservoir via smaller pores. Therefore, the propagation of the freezing front from the outer frozen phase is delayed till the moment when the temperature is low enough to freeze the smaller pores, referred as to necks. The phenomenon is often referred to as the pore blocking. Consequently, after freezing the neck at a certain T , the larger pore will freeze immediately at the same T . The situation described above leads to the complication in the determination of the freezing temperatures interrelated with each individual pore segment. Therefore, the genuine PSD determination from the freezing data is distorted. The thus calculated pore size distribution show the neck size distribution, rather than the whole spectrum of the pore sizes.

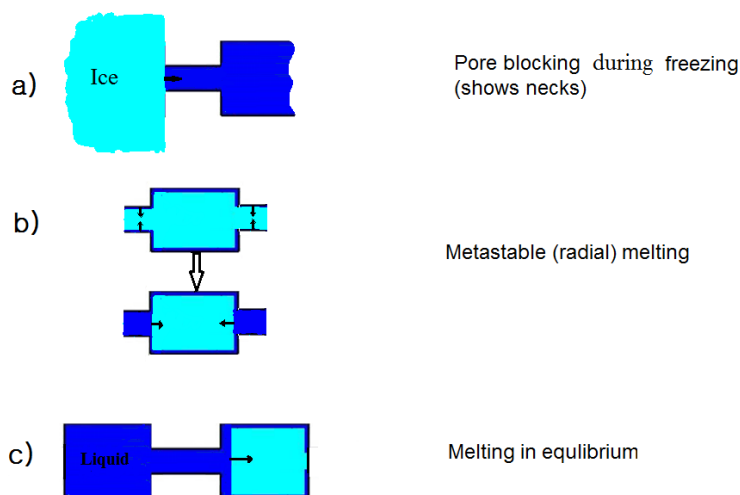


FIGURE 2.5: Different scenarios for the freezing and melting transitions. In dark colors the liquid phase and in light color the ice phase are shown.

The melting process differs from the freezing one by the existence of a molten layer on the inner pore surface, which plays a role of a nucleation seed for melting. In the case of small pores and narrow PSD, Figure 2.5b, the pores cannot melt at the equilibrium transition temperature, because there are no liquid domains spanning

over whole pore segments. The formation of such liquid domains is presented by the barriers in the free energy between the state with one molten layer coexisting with the frozen core and the state with completely molten pore. Therefore, the temperature first should be increased to a temperature higher than T_{eq} . When above-mentioned barrier is surpassed, the melting occurs at the same temperature radially towards to the pore center as it is shown by arrows. This situation is referred to as the metastable radial melting.

For larger pores and wide PSDs, the interplay in sizes between the pores can lead to the situation when, after melting in small pores at some T , the rest of them melts at the equilibrium temperature, Figure 2.5c. Thus, the metastability is removed due to the molten phase in the smaller pores and melting occurs via the melting front propagation in the axial direction. This situation is referred to as the melting under equilibrium.

The occurrence of different above-described scenarios leads to the different values of k factor in the Gibbs-Thompson equation. For freezing and melting under equilibrium, k factor is 2 times larger than that for the metastable melting [21]. In other words, the Gibbs-Thompson Eq. (2.14) is modified:

$$T_{fr}(x) = T_0 - \frac{4vT_0\gamma_{sl}}{Hd_c} = T_0 - \frac{2k}{d_c} \quad (2.16)$$

for freezing and melting under equilibrium and:

$$T_m(x) = T_0 - \frac{2vT_0\gamma_{sl}}{Hd_c} = T_0 - \frac{k}{d_c} \quad (2.17)$$

for metastable melting. Here, H is the heat of fusion, T is the temperature, T_0 is the bulk melting temperature, v is the molar volume, γ_{sl} is the surface energy.

It may be mentioned that different freezing-melting scenarios were considered in numerous works [21, 22, 23]. In real materials, like disordered porous glasses, the freezing-melting behavior can be complicated by the interplay of all mechanisms described and the determination of genuine pore size distributions may be highly obstructed. A more comprehensive analysis may be performed, for example, by using the so-called scanning technique together with computer simulations [22].

Considering Eq. (2.14), one may conclude that NMR cryoporometry has some limitations, such as maximal pore sizes accessible in thermoporometry experiments. On the other hand, micropores, i.e. pores with sizes less than 2 nm, are able to

accommodate only several molecules of liquid. It is, therefore, difficult to speak about crystal lattice of ice under these conditions. Thus, such small pores are also inaccessible for the analysis.

On considering a typical workflow of NMR cryoporometry experiments, they include in particular the initial temperature calibration. This is done using thermocouple Pt100. The accuracy of the temperature control for our setup is 0.2 K. Low temperatures are achieved by evaporation of liquid nitrogen. Before an NMR signal measurement, upon every change in temperature, 10-20 minutes is given for equilibration. We also have some additional tools to control the equilibration, thereby to provide the reproducibility of experiments. For NMR cryoporometry we applied mostly Hahn echo sequence (its description is given in the part devoted to PFG NMR) or Car-Purcell-Meiboom-Gill (CPMG) sequence to measure signal intensities.

Adsorption techniques were used additionally for a comparative structural characterization. It makes use of Kelvin equation, which is essentially similar to Gibbs-Thompson, to calculate pore sizes.

Chapter 3

NMR in Heterogeneous Systems

3.1 Diffusion in Crowded Media

3.1.1 Anomalous Diffusion in Dextran Solutions

Molecular transport in biological systems, such as ordinary cells (Figure 3.1) plays a decisive role in functioning of living organisms [24]. A cell may contain thousands of different types of proteins making concentration up to 300-400 mg/ml. Such concentrations lead to the phenomenon of molecular crowding. According to [25]: "Molecular crowding is more accurately termed the excluded volume effect, because the mutual impenetrability of all solute molecules is its most basic characteristic". It results in much more complex behavior in vivo in comparison to the conventional physical solutions. There are some clear evidences, that the rates of molecular rearrangement and, therefore, of biochemical reactions are strongly affected by this phenomenon. For instance, transcription and DNA replication could be to some extent ruled by effect of molecular crowding.

In particular, there are many experimental evidences that translational dynamics of various cell constituents may undergo sub-diffusion [26-38]. As an example, in work of Weiss et al. [8], the diffusion of labeled dextran molecules in cytoplasm of HeLa cells was investigated, revealing the subdiffusive motion with different anomaly parameters α in the range 0.6 - 1. It has been proven that molecular crowding is responsible for this behavior rather than other structural elements of the cell like endoplasmic reticulum - the random reticular network or microtubuli and actin filaments.

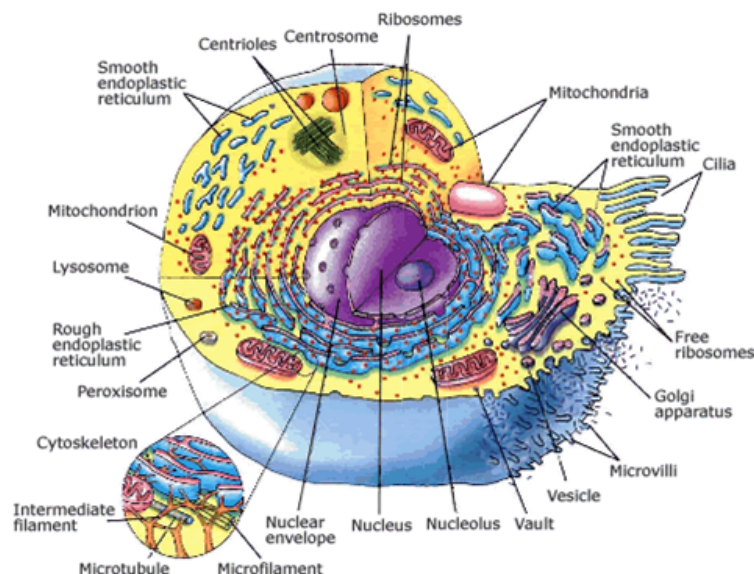


FIGURE 3.1: Image of a typical biological eukaryotic cell.

Since it is quite difficult to measure the diffusion processes in vivo, one of possible solution would be the attempt to find a model system. Anomalous diffusion is shown to occur already in systems containing not more than two differently sized macromolecules which may be considered as the simplest model mimicking cells [29, 30]. Taking two polymers with different molecular weights, where the heaviest one plays a role of crowding agent, and dissolving them in a solvent, for instance in water, one may follow the diffusion of the light component under crowding condition. Application of the fluorescence correlation spectroscopy (FCS) to aqueous solutions of two differently sized dextrans, with well-established procedure of data analysis, provided a clear evidence that the smaller one of dextrans undergoes subdiffusion [39, 40]. By combining the results of FCS with simulations, the properties of crowding-induced subdiffusion are shown to be consistent with the prediction for fractional Brownian motion or obstructed (percolation-like) diffusion and to notably deviate from the patterns expected for the continuous-time random walk [35, 41-43]. Further, the subdiffusive patterns observed have been suggested to result from anticorrelations in the course of Brownian motion having viscoelastic origin [44, 45].

Figure 3.2 shows the results obtained by fluorescence correlation spectroscopy for 3 different diffusing species in a solution of 500 kDa dextran (crowding agent) dissolved in water. As one may see, the 40 kDa dextran, shown by asterisk, undergoes a highly-pronounced anomalous subdiffusion already at low concentrations of crowding agent. This effect was detected for two other diffusion species,

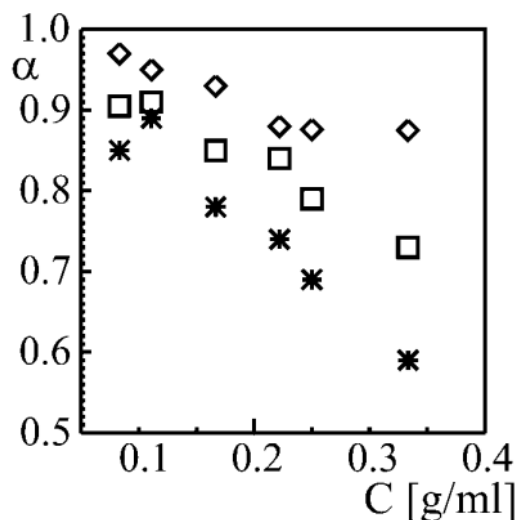


FIGURE 3.2: The dependence of anomaly parameter α on the macromolecular concentration of crowding agent (dextran with molecular weight 500 kDa). Dextran molecules with different molecular weights (diamonds, 10 kDa; asterisks, 40 kDa; squares, 500 kDa) chosen as diffusing agents. The figure is taken from [8].

although not so strongly pronounced. As a consequence of substructure formation, subdiffusion under molecular crowding is observable over distances exceeding the size of the involved molecules by more than 2 orders of magnitude [8]. With the further increasing of diffusion path lengths, the central limit theorem of statistics suggests the final transition to normal diffusion. This is expected as soon as the displacements notably exceed the correlation lengths of structural heterogeneities. In this case, the total diffusion path length may be understood as the superposition of displacements in subsequent intervals of time with identical probability distributions, giving rise to a Gaussian with a mean square width increasing linearly with time. The transition between subdiffusion and normal diffusion may be taken, therefore, as the measure of the correlation lengths of the substructures formed by molecular crowding.

Our objective was to study this phenomenon by another experimental technique, using the whole ensemble of diffusing molecules and to gain in this way some additional information about the microscopic origin of anomalous diffusion. The NMR technique is especially suitable in this case, because both polymers (heavy and light) are found in considered solutions in significant amounts, giving rise to strong NMR signals. Thus, 1H PFG NMR experiments can be performed with a sufficiently high accuracy.

3.1.2 Experiments and Discussion

In our work, we have also used dextran as a model polymer. Dextran is a complex, branched glucan (polysaccharide made of many glucose molecules) composed of chains of varying lengths. Its molecular weight can approach 1 MDa.

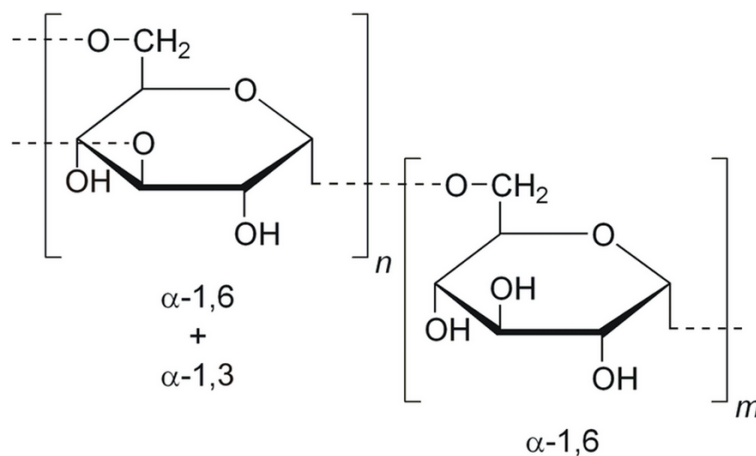


FIGURE 3.3: Structure of a dextran molecule.

The PFG NMR measurements have been done with 40 and 640 kDa dextrans (Sigma-Aldrich, Germany) dissolved in deuterated water. Heavier dextran played a role of crowding agent. As a first step, both of dextrans were prepared as single component solutions of 5 wt % in order to follow their diffusion dynamics independently.

Figure 3.4 shows the PFG NMR signal attenuation curves as the primary data of the PFG NMR diffusion studies for the pure components (both of 40 kDa and 640 kDa dextrans) dissolved at 5% weight concentration in deuterated water.

For a single-component system undergoing normal diffusion with a diffusivity D , the PFG NMR attenuation curve is known to follow a simple exponential Eq. (2.13) [46, 47]. The attenuation curves shown in Figure 3.4 are clearly seen to not comply with such simple pattern.

The most obvious reason for such observation is a distribution of molecular masses of the polymers in our study. Therefore, we have to take into account, that, as a consequence of mass distribution inherent to each of the dextran samples, there is also a distribution $p(D)$ in the diffusivities of each component [48, 49]. Although $p(D)$ is generally not known, it is often approximated by the log-normal distribution [50]:

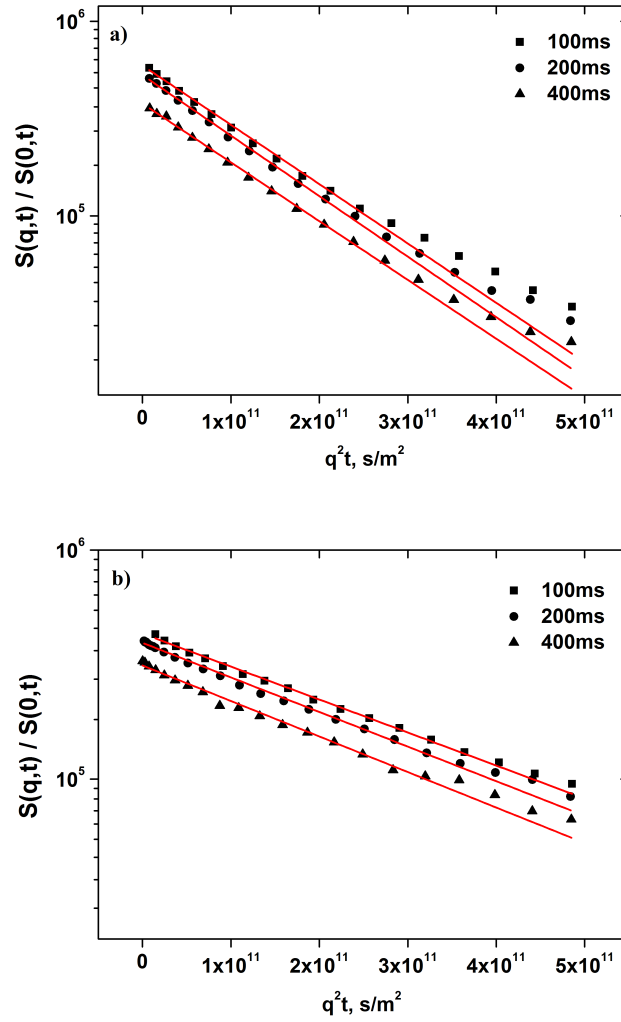


FIGURE 3.4: Spin-echo diffusion attenuation functions for 40 kDa (a) and 640 kDa dextran (b) aqueous solutions measured at different observation times. The solid lines show the best fit of Eq. (2.13) to the experimental data, i.e. their slopes correspond to the diffusion coefficient.

$$P(D) = (\sqrt{2\pi D\omega})^{-1} \exp\left(-\frac{(\ln D - \ln D_0)^2}{2\omega^2}\right) \quad (3.1)$$

where D_0 is the average diffusivity and ω is the distribution width. Under such conditions, the PFG NMR signal attenuation results as a superposition:

$$\Psi = \int P(D)\Psi_s(D)dD \quad (3.2)$$

rather than as a single exponential, where Ψ_s is given by:

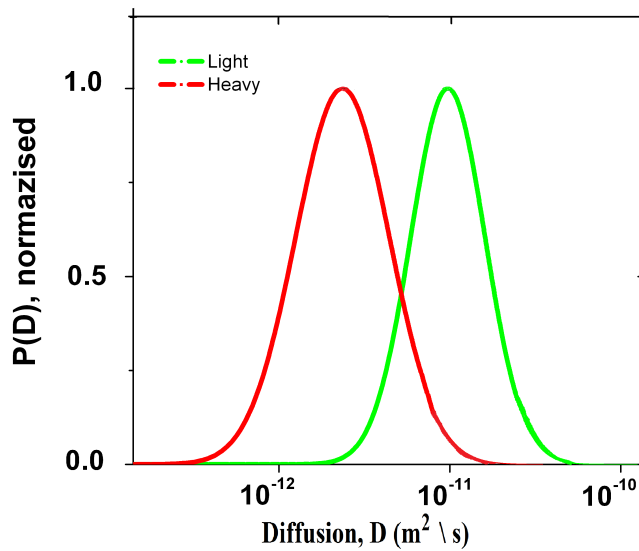


FIGURE 3.5: Normalized diffusivity distribution functions $P(D)$ for light (40 kDa) and heavy (640 kDa) dextrans, obtained by fitting Eq. (3.1) to the experimental data from Figure 3.4.

$$\Psi_s = \Psi_0 \exp(-q^2 Dt) \quad (3.3)$$

During the next step we evaluated the possible overlap in diffusivities of 40 kDa and 640 kDa dextrans. The Figure 3.5 shows the normalized diffusivity distribution functions for the two single-component 5% aqueous solutions of dextrans obtained by fitting Eq. (3.2), combined with Eq. (3.1) and Eq. (3.3) to the experimental data. It has to be mentioned that Ψ_0 , which takes account of the transverse and longitudinal rates of nuclear magnetic relaxation of the polymer molecules, has been taken to be identical for each mass fraction. In our case, due to the high dilution of dextran molecules and the relatively narrow mass distributions, this is well-justified [51]. Notably, the distributions $p_{light}(D)$ and $p_{heavy}(D)$ resulting for the two different dextran samples with the molecular masses of 40 kDa and 640 kDa, respectively, do not overlap heavily and can thus be easily separated from each other in the PFG NMR diffusion measurements with two components in a mixture (given that, in the mixture, the diffusivities will remain not notably changed).

The third sample studied consisted of a 75% 640 kDa to 25 % 40 kDa mixture in an aqueous solution of 20 wt %. Among the various dextran mixture compositions considered in [29, 30], the latter composition was selected as a compromise

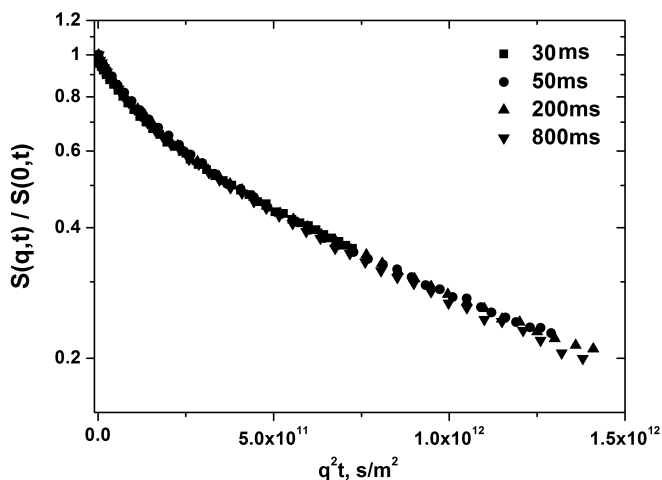


FIGURE 3.6: Normalized spin-echo diffusion attenuation functions for the 20 % aqueous solution of dextran mixture (75 % of 640 kDa dextran and 25 % of 40 kDa dextran) for several diffusion times.

for attaining sufficiently large transverse nuclear magnetic relaxation times, necessary for enabling measurements over the considered time and space scales and still showing a notable anomaly according to [29]. Indeed, as it was described before (see Figure 3.2), this system shows the pronounced effect of anomalous subdiffusion.

Figure 3.6 presents PFG NMR attenuation curves for the two-component system for the total range of diffusion times $30 \leq t \leq 800$ ms studied in the experiments. The experimental error of our measurements does not exceed the symbol size. One may easily see that the diffusion time dependence, if exist, is very small. To prove it more accurately, as the next step, the diffusion attenuation curves for two most distant diffusion times (30 ms and 800 ms) were taken and compared in the same range of q^2t .

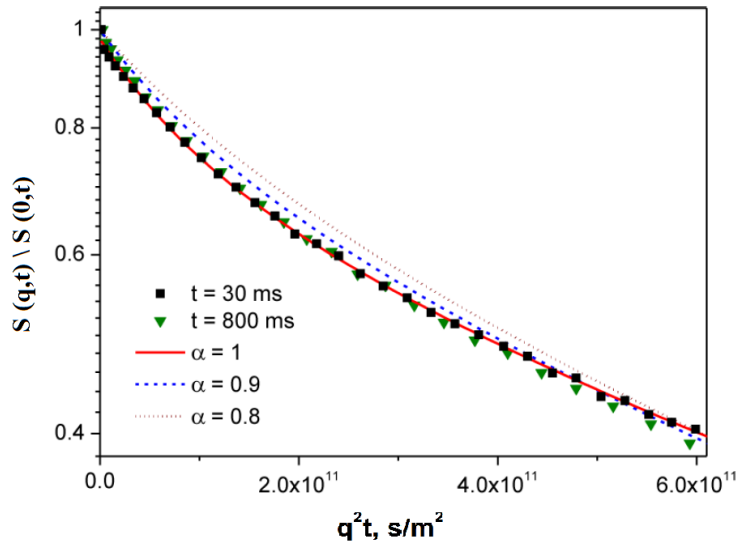


FIGURE 3.7: Normalized spin-echo diffusion attenuation functions for the 20 ”%” aqueous solution of dextran mixture (75 wt ”%” of 640 kDa dextran and 25 ”%” of 40 kDa dextran) for two diffusion times, 30 and 800 ms. The solid line shows the best fit of equation 3.3 to the experimental data. The broken lines show the attenuation curves resulting from the analytical expressions of Eq. (3.4), (3.2) and (2.6) for diffusion time = 800 ms, assuming subdiffusion with the exponents $\alpha = 0.8$ (dots) and 0.9 (dashes) for the lighter dextran component.

Full line in Figure 3.7 shows the attenuation curve obtained via Eq. (3.2) with a distribution function $p(D)$ as resulting from the weighted superposition of the distribution functions of the two constituents shown in Figure 3.5, namely:

$$\Psi = \sum \int f_i p_i(D) \Psi_i(D) dD \quad (3.4)$$

with the subscript i referring to the two dextran components (light and heavy), f_i denoting the proton fractions (in our case, coinciding with the weight fractions) of the two components, $p_i(D)$ as given by Eq. (3.1) with the distribution widths ω obtained from the single-component solutions, and $\Psi_i(D)$ as given by Eq. (3.2). In this way, we have assumed that, upon mixing, only the mean diffusivities $D_{0,i}$, of the mixture components do change, while their distributions, as compared to the single-component dextrans, remain invariant. It is shown by the solid line in Figure 3.7 that in this way, with only two fitting parameters $D_{0,i}$, an excellent fit of Eq. (3.1) to the experimental data is obtained.

As observed already with the single-component systems in Figure 3.4, the PFG NMR signal attenuation is found to be invariant with time. This result was indeed

expected for the single-component systems, which are implied to undergo normal diffusion. However, also the mixture data displayed in Figure 3.6 are now found to yield, within the limits of accuracy, no indication of a time dependency. For all observation times ($30 \leq t \leq 800$ ms), the best fit of the experimental attenuation data was attained with time-invariant diffusivities, namely, with values of $D_{light} = (8.7 \pm 1) * 10^{-12} m^2 s^{-1}$ and $D_{heavy} = (9.7 \pm 0.35) * 10^{-13} m^2 s^{-1}$ respectively, for the two dextran components.

To assess the significance of this finding, we have to check how strong the deviation of the time exponent α , from $\alpha = 1$ for normal diffusion, has to be for giving rise to a clearly visible splitting in the $\ln \Psi$ versus $q^2 t$ attenuation plots for different observation times. This is illustrated in Figure 3.7 by the dashed and dotted lines. They show the attenuation plots, which, on the basis of the data for $t = 30$ ms, must be expected for an observation time of $t = 800$ ms if the lighter dextran component had undergone subdiffusion with time exponents $\alpha = 0.9$ and 0.8 respectively. With Eq. (2.6) (see chapter 2 devoted to diffusion), in this case, the diffusivity for $t = 800$ ms would amount to:

$$D_{light}(t = 800 \text{ ms}) = 8.7 \times 10^{-12} m^2 s^{-1} \left(\frac{30 \text{ ms}}{800 \text{ ms}} \right)^{1-\alpha} \quad (3.5)$$

rather than $D_{light} = 8.7 \times 10^{-12} m^2 s^{-1}$, which holds for $t = 30$ ms. As expected from Eq. (2.6), the thus calculated PFG NMR attenuation plots for $t = 30$ ms must exhibit the faster decay with increasing observation time than it was observed in the experiment. Therefore, the comparison between the experimental data and the calculations clearly indicates that, over the considered space and time scales, subdiffusion with time exponent $\alpha = 0.8$ can be ruled out, while a value of $\alpha \approx 0.9$ can be considered as a reasonable lower limit. With Eq. (2.4), the minimum diffusion path lengths of the light dextran molecules in our experiments are found to be of about $1.2 \mu m$:

$$\sqrt{\langle r^2 \rangle} = \sqrt{6 \times D_{light} \times t_{diffusion}} = \sqrt{6 \times 8.7 \times 10^{-12} \times 30 \times 10^{-2}} \approx 1.2 \mu \quad (3.6)$$

Having in mind that the maximum path lengths covered in FCS, which are on the order of $0.5 \mu m$, provide clear evidence of subdiffusion with $\alpha \approx 0.8$, with the present findings, the transition from sub- to normal diffusion can be estimated to occur in exactly this intermediate range, that is, from about 0.5 to $1.2 \mu m$. Figure 3.8 summarizes the results of our investigations and results obtained by means of FCS. It shows a transition from the anomalous regime at short diffusion times to the normal diffusion regime for longer diffusion times.

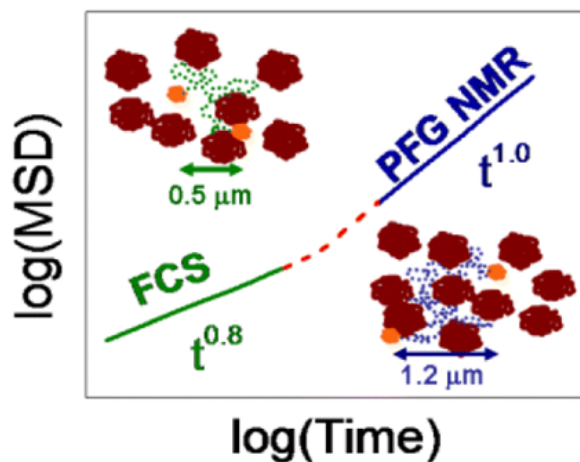


FIGURE 3.8: Summary of FCS and NMR studies.

In the present studies, the potentials of PFG NMR for tracing short displacements (down to 100 nm) could be only partially exploited. To close the existing gap between NMR and FCS techniques, one should look for a system that could reproduce the situation of molecular crowding and be accessible for both of them. Main drawback of the experiment presented here was the fact that we have analyzed the whole ensemble of molecules taking into account diffusion of both components. In contrast to FCS experiment, in PFG NMR molecules of both diffusant (light dextran) and obstacle (heavy dextran) were measured simultaneously. It imposed the additional difficulties on analysis of the data obtained. Therefore, the system with different components from the point of view of NMR is needed. First possibility could be to partially deuterate one of dextran and follow it (analogous situation as in the case of labeling in FCS). Unfortunately, the sensitivity of our setup did not allow using this trick, because deuterium provides very low signal. Another idea would be to use fluorine, which provides better signal, for labeling. Our estimations gave the limit of fluorination accessible in our measurement about 20%, i.e. 20% of hydrogen atoms in dextran should be replaced with fluorine atoms). The fluorination of a polymer is, however, a complex, multi-step task. Thus, a direct fluorination in the bulk phase of hexafluorobenzene led to the destruction of dextran.

Currently, we are collaborating with the group of Prof. Bräuchle from Munich University on a third approach in new samples, where the heavier dextran was partially immobilized by the cross-linking process. By varying the amount of a cross-linking agent, the degree of immobilization can be controlled upon the sample preparation. In this case, the diffusion of only light dextran can be followed. These experiments are in progress.

3.2 Investigation of Complex Fluids

3.2.1 Nematic Microemulsions

The microemulsions consisting of two immiscible liquids, like oil and water stabilized by a surfactant, attracted a lot of interest due to their unusual optical and rheological properties. Molecules of the surfactant have hydrophobic and hydrophilic ends. Therefore, in the presence of water they organize so-called micelles with hydrophilic ends inwardly directed to the water core and hydrophobic ends, which are directed outward. The thus formed micelles usually have sizes of order of micrometers and are dispersed in an oil phase, creating the colloidal phase.

Our work is devoted to the systems, where the oil phase is replaced by a liquid crystal to bring a spatial anisotropy that, in turn, results in very complex phenomena due to the emerging elastic interactions [52-55]. These interactions may give rise to a rich structural behavior determined by the local disturbances of the director fields close to the colloid surfaces [56-57]. In this part of the thesis, the advantages of NMR spectroscopy were used to investigate one particular kind of complex fluids, namely nematic microemulsions (NM). Yamamoto and Tanaka, using didodecyl dimethyl ammonium bromide (DDAB) as the surfactant and the phase of thermotropic liquid crystal (pentylcyanobiphenyl or 5CB), obtained the nematic microemulsion with micelles smaller by two orders of magnitude (about several nanometers) than for systems described above [10]. Moreover, the different local organizations in this material at different temperatures have been demonstrated. In particular, the existence of two phase transitions upon varying temperature has been shown using differential scanning calorimetry. First transition occurred around 31 °C, where isotropically orientated molecules of liquid crystal have formed a nematic star-like (surfactant molecules are directed towards the center of a micelle) phase around micelles on the length scale of the micellar size. At the same time, the system remained isotropic on a larger scale. This local ordering was attributed to the existence of a strong directional coupling between the LC and the surfactant molecules. Remarkably, the whole system remained transparent, i.e. the light is not affected by local ordering. This literally means that the whole system is macroscopically isotropic, but locally has the nematic order. It was called a new phase - transparent nematic (TN) phase. Further, under the temperature decrease, the second transition occurred. Near 29 °C, the temperature of isotropic-nematic transition for liquid crystal in bulk, the system became turbid. It was associated with the formation of the nematic phase of liquid

crystal. TN phase continued to exist and both phases separated macroscopically after several hours. Under the gravity force, the heavier liquid crystal displaced downwards and the transparent nematic phase containing micelles floated to the top of the sample.

In the series of consequent works [11, 58], the existence of a local order was questioned. Deuteron nuclear magnetic resonance (DNMR) microimaging has shown that the presence of micelles only slightly diminishes the local nematic order parameter [11]. Moreover, some attempts to establish the mechanisms driving the macroscopic phase separation were undertaken. Bellini et al. have employed static and dynamic light scattering measurements to follow separately contributions from paranematic fluctuations and from the micelles [59]. Based on the experimental results obtained, it has been suggested that the fluctuations in the orientational ordering are responsible for the attractive interaction of the micelles, finally leading to the macroscopic separation. One of the evidences for the attractive interaction was drawn from the observation of the slowing down of the micellar diffusivities, namely a finding that the experimentally determined diffusivities slow down faster with decreasing temperature than those predicted on the basis of the Stokes-Einstein equation. It was considered as an indication that the attractive interaction between the micelles becomes effective before the temperature of the isotropic-nematic transition is approached. These findings were further supported by small angle neutron and X-ray scattering experiments [13]. They, first of all, confirmed the occurrence of the nanometer-sized inverse micelles of a spherical shape. Secondly, the experiments revealed an increase of paramagnetic fluctuations upon approaching the isotropic-nematic transition temperature.

The interactions determining the structural organization of such prepared systems as well as their complex behaviors upon temperature variation are still a matter of consideration. For nematic emulsions with colloid sizes of the order of micrometers, the dominant interactions were associated with the LC anchoring energy on the colloid particle surfaces and the LC elastic energy [60]. For nanosized colloid particles, however, the anchoring is not fulfilled anymore, and the dominant interactions are expected to be controlled by Wan der Waals interaction, paranematic fluctuation and Casimir forces [13].

In all these works, a particular attention has been paid to the understanding microscopic dynamics of the mixture components and to using this information for a better understanding of the structure formation and the system behavior. The pulsed field gradient technique of nuclear magnetic resonance is proven to be the

most powerful experimental method to probe directly the rates of molecular propagations under equilibrium conditions [61-62]. Being very sensitive to molecular rearrangements on the time scale from a few microseconds to a few thousands of milliseconds, it may provide a complementary information about dynamic processes occurring in soft-matter [63]. Its potentials are exploited here to get deeper insight into the microscopic dynamic of the LC-microemulsion complexes.

The LC-microemulsions mixtures used in this study were composed of 4'-Pentyl-4-biphenylcarbonitrile (5CB, $CH_3(CH_2)_4C_6H_4C_6H_4CN$) liquid crystal, surfactant didecyltrimethylammonium bromide (DDAB, $[CH_3(CH_2)_9]_2N(CH_3)_2Br$) and water. The LC (98 % purity) and surfactant (98 % purity) were purchased from Sigma-Aldrich (Germany) and used as it is, without further purification. We quantify the composition of the samples under study in terms of the weight fraction φ of DDAB+water in lyotropic crystal (5CB). This defines an intermicellar distance d :

$$d = a \times (4\pi/3\varphi)^{1/3} \quad (3.7)$$

where a is a micellar radius. The latter is given as

$$a = \delta(3 - 2\phi)/\phi, \quad (3.8)$$

where ϕ is a weight fraction of DDAB in the micelle (DDAB+water) and δ is a length of the surfactant molecule (~ 1.25 nm). Molecules of liquid crystal are about 2 nm long.

In what follows, the composition-relevant parameters will be used to label the samples prepared: first letter M stands for sample, the second letter shows whether water presents in the sample (protonated H or deuterated D) or not (x). The number used corresponds to the parameter φ , which defines the micellar concentration.

Sample	Mass of 5CB, g	Mass of DDAB, g	Water, g	ϕ	a, nm	φ	d, nm
MD15	0.1485	0.02	0.006	0.77	2.37	0.15	7.2
Mx13	0.1518	0.022	-	1	-	0.13	4
MD6	0.1530	0.008	0.0012	0.87	1.81	0.06	7.45
MH8	0.1467	0.011	0.0015	0.88	1.76	0.08	6.58

TABLE 3.1: The sample characteristics under study with calculated values of the radius and the intermicellar distance.

In the present work, four samples with different compositions were studied. The formation of micelles earlier was proven to occur in the range of the mass concentrations between 5 and 15 weight % of surfactant plus water in LC [13]. Therefore, we prepared two samples (MD15 and MD6) with the mass fractions representing two limiting cases of the weight fractions where the TN phase is still observed. Because ϕ determines the micellar size, in this way, the effect of the micellar size could be addressed by comparing the results obtained with these two samples. A sample (Mx13) contained roughly the same amount of DDAB as in MD15, but no water, to exclude the formation of micelles. In this way, the transport of individual DDAB molecules in the LC could be probed. Since, in the literature, normal and heavy water were frequently and equally used in the experiments without any remark about the possible difference in their properties, we decided to check a possible effect of water chemistry and prepared the sample MH8, with similar weight fraction as in case of MD6, but using normal (protonated) water instead of deuterated. Calculated populations (proton fractions) for all samples are presented in Table 3.2.

Sample	P_{5CB}	P_{DDAB}	P_{water}
MD15	82.8	17.2	0
Mx13	81.7	18.3	0
MD6	92.5	7.5	0
MH8	88.4	10.3	1.3

TABLE 3.2: Proton fractions (in %) of every component contributing to NMR signal for all samples under study.

The visual representation of the mesostructure of the samples prepared is shown in Figure 3.9. It is important to mention that every sample before measurement was preliminarily stirred in an ultrasound bath at high temperature (60 °C). As it was shown in [11], the initial state of the system is not easily reproducible upon simply shaking the samples. Therefore, the same procedure of the sample homogenization was repeated in our experiment every time before any measurements were done.

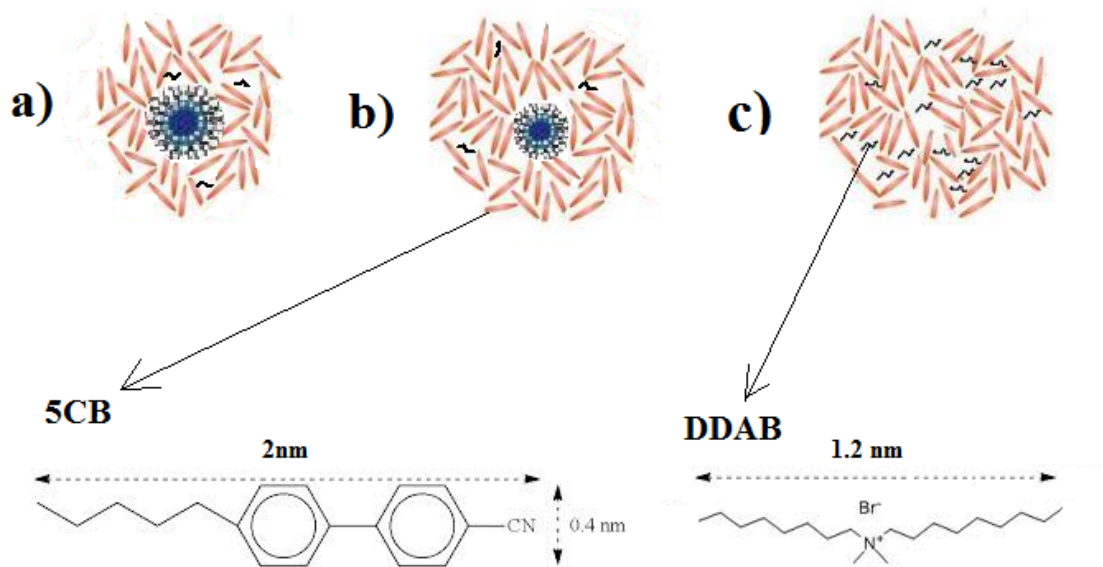


FIGURE 3.9: Schematic representation of the structure of three samples studied: (a) MD15, (b) MD6, and (c) Mx13. The figures a) and b) show effective unit cells according to the data of Table 3.1.

Before presenting the results of diffusion study of the complex mixtures, we provide, for comparison, the data obtained for the pure LC.

Notably, with the conventional NMR technique, such measurements are possible only in the isotropic phase of LC, since it requires sufficiently long times τ to incorporate the magnetic field gradients and during which the nuclear magnetic spin-spin relaxation processes occur. In the nematic phase with very short spin-spin relaxation times this type of simple experiments is, therefore, not possible. In the isotropic state of LC above T_{IN} , the dipole-dipole interactions between the LC molecules are effectively averaged out due to an irregular molecular tumbling, yielding relatively long relaxation times, $T_{2,LC}$, henceforth measurable NMR signals. Due to increasing molecular ordering, averaging becomes more and more incomplete upon approaching the isotropic-nematic transition, giving rise to a strong decrease of $T_{2,LC}$, precluding thus NMR experiments. The more complex experiments can, however, be performed under this condition [64-66]. In the measured range of temperatures, the NMR spin-echo attenuations (see Figure 3.10) are found to have exponential shapes described by Eq. (2.13). The diffusivities

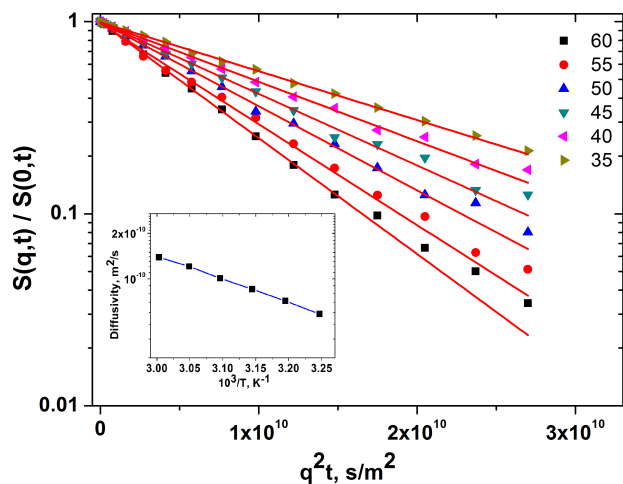


FIGURE 3.10: Normalized spin-echo diffusion attenuations for 5CB in the isotropic phase for the selected temperatures (in $^{\circ}\text{C}$). The inset shows the Arrhenius plot of the diffusivities, resulting activation energy for diffusion is 29 kJ/mol.

determined by fitting Eq. (2.13) to the experimental data are shown (inset in Figure 3.10) and are found to be in a good accord with the literature data reported earlier [64].

3.2.2 Diffusion in Liquid-Crystal Microemulsion.

Applying the above-described preparation procedure, we recorded the spin-echo diffusion attenuation curves. After every temperature change, enough time (30 minutes) was given to the system to equilibrate. The attainment of equilibration was proven by applying Hahn sequence with help of which the signal evolution with time can be followed. It has been waited until no notable change of signal intensity was observed.

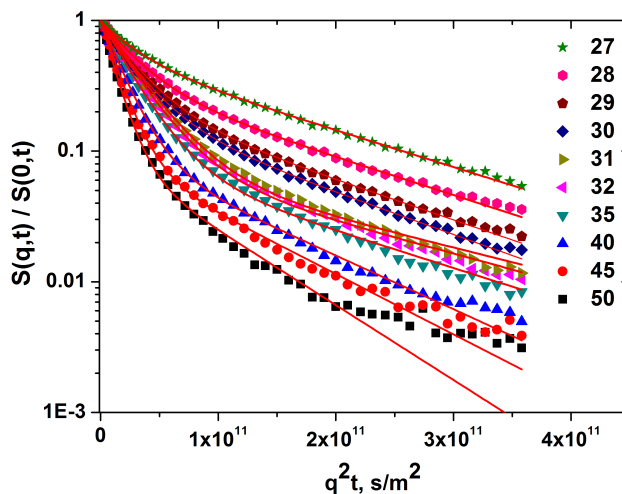


FIGURE 3.11: Normalized spin-echo diffusion attenuations measured in the sample MD15 for the selected temperatures (in $^{\circ}\text{C}$). The lines show the best fit of Eq. (3.9) to the experimental data.

Figure 3.11 shows the spin-echo attenuation curves for the sample MD15 measured at different temperatures. They turned out to have multi-exponential shapes. This is observed for all temperatures, including the highest one, where the system is expected to be in a macroscopically homogeneous state. Since the both ensembles of molecules (liquid crystal and surfactant) contribute to the measured NMR signal (both of them contain protons), the overall signal $S(q, t)$ is determined as a sum of two components:

$$S(q, t) = P_{LC}(0, t) \times \exp(-q^2 D_{LC} t) + P_{DDAB}(0, t) \times \exp(-q^2 D_{DDAB} t) \quad (3.9)$$

where the fractions $P_i(0, t)$ are defined as

$$P_{LC}(0, t) = S_{LC}(0, t) / (S_{LC}(0, t) + S_{DDAB}(0, t)) \text{ and}$$

$$P_{DDAB}(0, t) = S_{DDAB}(0, t) / (S_{LC}(0, t) + S_{DDAB}(0, t)).$$

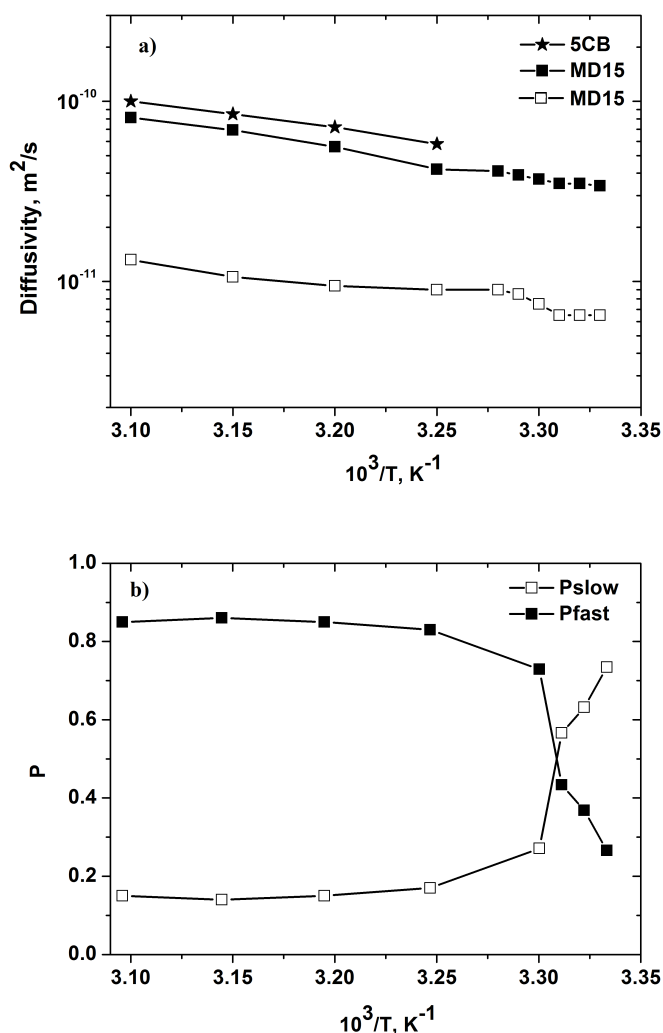


FIGURE 3.12: Arrhenius plot of the diffusivities of 5CB (filled symbols) and of DDAB (open symbols) in MD15 and the corresponding populations resulting from the fit of Eq. (3.9) to the experimental data. The data for the diffusivities of 5CB in bulk are shown by stars for comparison.

Thus, since the diffusivities of DDAB and LC are notably different, the shape of $S(q, t)$ can be approached by the two-exponential fit (Eq. 3.9). The weights $P_{LC}(0, t)$ and $P_{DDAB}(0, t)$ are found to be strongly temperature dependent. Most notably, in contrast to the pure LC sample, the PFG NMR measurement could now be performed for temperatures well below T_{IN} (see Figure 3.12). It turns out that the presence of additive species provides enough disorder effects to give rise to the NMR signals on the time scale of PFG NMR experiments.

The results of the fitting of Eq. (3.9) to the experimental data for the sample MD15 are shown in Figure 3.12. Importantly, the calculated proton fraction in the sample for DDAB is $\sim 17\%$. As one may see from Figure 3.12b, at the high

temperatures, before the nematic - isotropic transition is expected to occur, the population of the slow component coincides with the calculated proton fraction with very high accuracy. The same is true for LC component. Therefore, we can directly associate the diffusivities of the slow and the fast diffusing components with the diffusivities of the surfactant and LC components, respectively. As one can see from Figure 3.12a, the faster diffusing component is only slightly slower than the diffusivity in the bulk phase of 5CB at the temperatures above the isotropic-nematic transition temperature. Quite formally, this can be attributed to the hindering effect of the micelles upon the LC molecules. The diffusivity of the slow component, corresponding to the micelles, is notably smaller than the diffusivity of the fast component, making both of them easily distinguishable. To the best of our knowledge, it is the first direct measurement of diffusion coefficient for both components in nematic microemulsions of such kind. It may be noted, that, upon crossing the isotropic-nematic transition temperature, the character of the temperature-dependency, which may be approximated by an Arrhenius-like behavior, changes only weakly. This may be quantified, e.g. by noting the lowering of the activation energy for $T < T_{IN}$ if the data above and below T_{IN} are approached by the Arrhenius law, i.e. $D \propto \exp(-E_A/kT)$, where E_A is the activation energy of diffusion and k is the Boltzmann constant. It may be noted that macroscopic changes occurred around T_{IN} . Upon the lowering temperature below T_{IN} the sample MD15 phase separates. It can be detected by simple visual observations. Thus, the stability of the system is broken and the micelles are expelled into micelle-rich phase to the top of the sample. The bottom part contains almost purely liquid crystal, which is upon the lowering temperature shows a transition to the nematic phase. It leads consequently to the disappearance of the NMR signal due to shortening of the T_2 relaxation times of the LC molecules in the nematic phase. With further lowering of temperature, the signal disappears completely.

Although, as it was mentioned above, the existence of micelles has been proven in a number of experiments, an additional cross-check has been accomplished. Figure 3.13 shows the spin-echo attenuation functions $S(q, t)$ for two samples MD15 and Mx13, with and without water, for selected temperatures around T_{IN} . Importantly, no dependency of $S(q, t)$ on the diffusion time was detected. This fact is a strong indication of a homogeneous character of the diffusion processes occurring in the sample on the time scale of the diffusion experiments. Although the shapes of $S(q, t)$ for two samples are qualitatively similar, as determined by the contribution of two diffusing species, a notable difference in the variation of their relative weights to the overall signal is observed. In the case of Mx13, $P_{LC}(0, t)$ does not

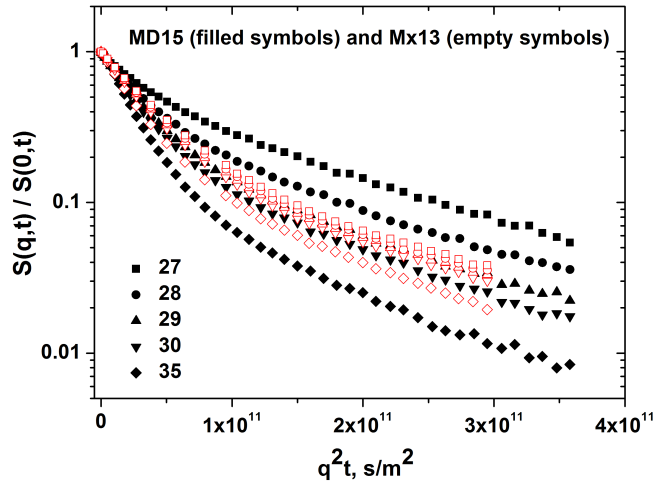


FIGURE 3.13: Normalized spin-echo diffusion attenuations for the samples MD15 (filled symbols) and Mx13 (open symbols) measured at different temperatures.

change appreciably with decreasing temperature, revealing the minor structural ordering in the sample. Recalling that the strong ordering of 5CB in the sample MD15 was possible due to the macroscopic phase separation process, this phenomenon can be ruled out to occur for the sample Mx13. Upon the decreasing of temperature to the room temperature, the system remained stable and uniform. The diffusivity behavior of DDAB will be addressed in the next section.

To get further insight into how the microscopic dynamics in the systems considered is correlated with their structural properties, namely with their composition, the sample MD6 with the water content lower than in MD15 was studied, where the micellar size is smaller. Notably, the composition of this sample is such, that it also exhibits the macroscopic separation for $T < T_{IN}$. This is as well supported by the experimental results shown in Figure 3.14, indicating the identical behavior of the NMR spin-echo diffusion attenuations as in the sample MD15.

As it follows from the comparison of the spin-echo attenuations shapes in Figure 3.14, the fraction $P_{DDAB}(0, t)$, corresponding to that of the slow diffusing component in $S(q, t)/S(0, t)$, changes more strongly in the sample MD6 with decreasing temperature. This may qualitatively be correlated with the lower content of the microemulsion in the sample. The latter determines (i) the higher relative volume of the LC-rich phase in MD6 as compared to MD15, and (ii) the lower relative amount of the DDAB molecules in the LC-rich phase. The both features contribute to the stronger ordering of the LC molecules at one and the same temperature, hence, to lower transverse nuclear magnetic relaxation rates in the LC phase. At

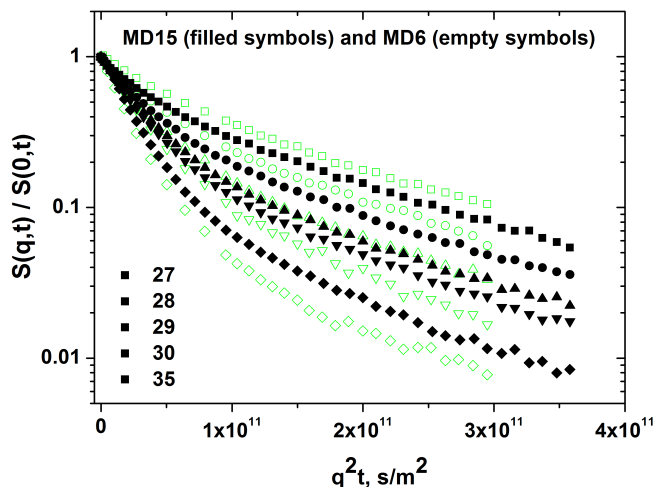


FIGURE 3.14: Normalized spin-echo diffusion attenuations for the samples MD15 (filled symbols) and MD6 (open symbols) measured at different temperatures.

the temperatures substantially higher than T_{IN} , $P_{DDAB}(0, t)$ is predominantly determined by the mixture composition, not by the nuclear effects. Because the fraction of DDAB in MD6 is lower than in MD15, $P_{DDAB}(0, t)$ in Figure 3.14 for $T > T_{IN}$ is also found to be lower. The calculated proton fractions and that obtained in the experiments coincide within the limits of accuracy (see Table 3.2). With decreasing temperature, however, the stronger ordering of the LC molecules in MD6 gives rise to a notably stronger decrease of $P_{LC}(0, t)$ or, correspondingly, to a stronger increase of $P_{DDAB}(0, t)$ in full agreement with the experimental findings. On the other hand, the diffusivities of both LC and DDAB do not show any appreciable (within the experimental accuracy) dependency on the system composition for $T > T_{IN}$. Only some minor differences may be noted to occur for $T < T_{IN}$.

All experiment described above were performed with the microemulsions containing deuterated water. This has been purposefully done to exclude the water contribution to the measured 1H NMR signal (even though its proton fraction is estimated to be $\sim 1\%$). In order to check whether this substitution could affect the system properties, i.e. to exclude the isotopic effect on the system structuring, some additional studies were made using normal water. The overall composition of this sample, MH8, was relatively close to that of MD6. The comparative NMR spin-echo diffusion attenuation functions shown in Figure 3.15 as well as the diffusivities of LC and DDAB shown in Figure 3.17 for selected temperatures around

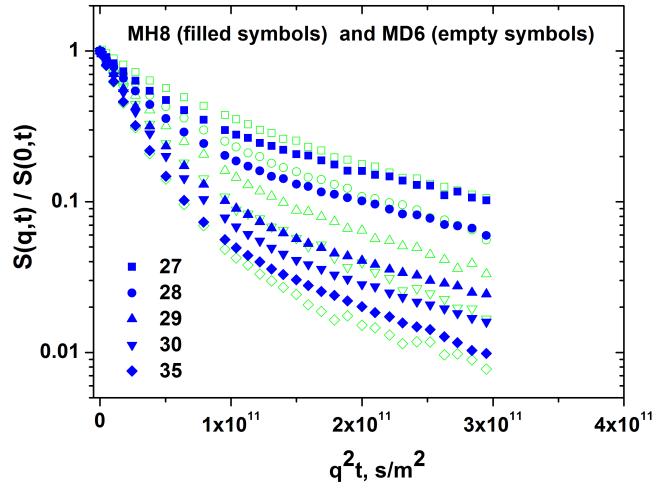


FIGURE 3.15: Normalized spin-echo diffusion attenuations for MH8 (filled symbols) and MD6 (open symbols) measured at different temperatures.

T_{IN} reveal qualitatively similar behavior. This means that all conclusions drawn so far are equally valid for the microemulsions containing normal water.

The diffusivities obtained by fitting Eq. (3.9) to the data of Figure 3.11 and Figure 3.14 are shown in Figure 3.16. Notably, the diffusivities of 5CB in Mx15 are found to be smaller than in the sample MD15. At the same time, it is quite remarkable that the diffusivities of DDAB are found to be almost identical to those in MD15 at $T > T_{IN}$ and are only slightly lower than those for $T < T_{IN}$. Let us discuss these two findings concerning the diffusion behavior of the two mixture components separately.

Firstly, the minor effect of the micelles formation upon translational mobility of the DDAB molecules, can only be rationalized by appreciating a highly dynamic nature of the individual micelles in terms of very short retention times of the individual molecules in the micelles as compared to the time scale of the PFG NMR experiments above 1 ms. Indeed, the overall displacements $\langle r^2(t) \rangle$ of the DDAB molecules can quite generally be estimated as

$$\langle r^2(t) \rangle = (\tau_{ind}/t) \langle r^2(t) \rangle_{ind} + (\tau_{mic}/t) \langle r^2(t) \rangle_{mic} \quad (3.10)$$

where τ_{mic} and τ_{ind} denote the time spans within the time interval t , during which the DDAB molecules diffuse as parts of the micelles and as the individual entities in the LC phase, respectively. $\langle r^2(t) \rangle_{mic}$ and $\langle r^2(t) \rangle_{ind}$ stand for the

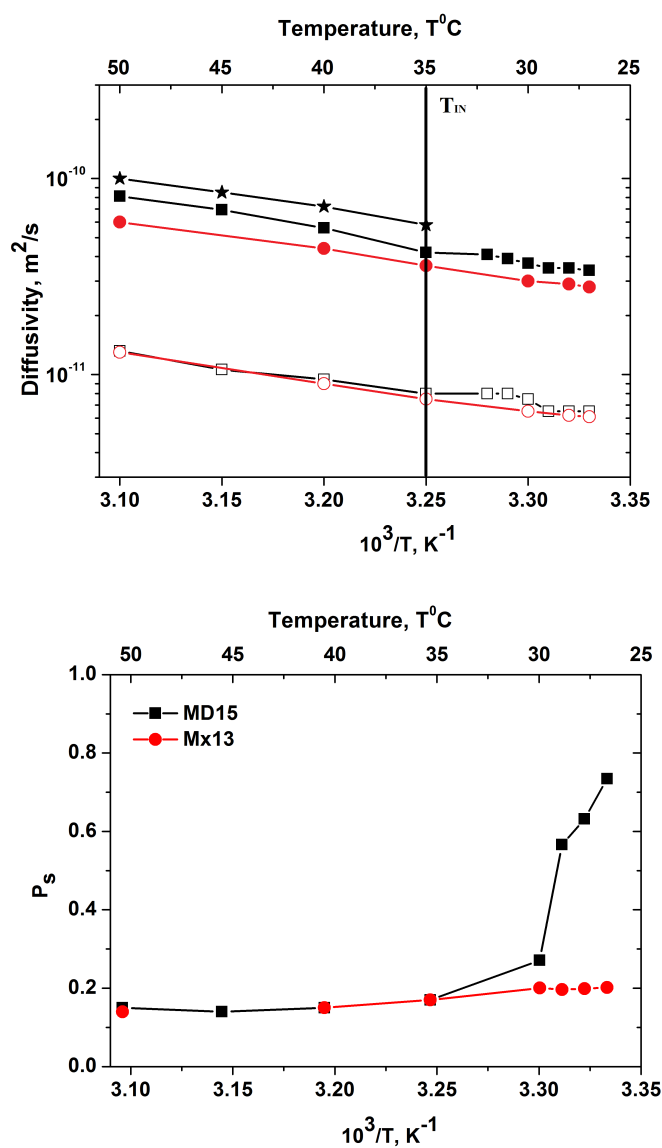


FIGURE 3.16: Diffusivities of 5CB (in bulk (stars), in MD15 (filled squares), and in Mx13 (filled circles)) and of DDAB (in MD15 (open squares) and in Mx13 (open circles)). The corresponding fraction P_s of the surfactant component obtained using results of the fitting of Eq. (3.9) to the experimental data are shown in b. It reveals no change in the population for the sample Mx13, because the phase separation does not occur in this case.

respective mean square displacements acquired during these time intervals. Notably, τ_{ind} (the same refers equally to τ_{mic}) may be composed of many shorter events of the diffusive excursions in the LC phase. In writing Eq. (3.10), it was reasonably assumed that any memory effects between such subsequent trajectories are negligible. By dividing the both sides of Eq. (3.10) by $6t$ and by introducing $P_{DDAB,LC} = \tau_{ind}/t$ and $P_{DDAB,m} = \tau_{mic}/t$, one obtains the effective diffusivity

$$D_{DDAB,eff} = P_{DDAB,LC}D_{DDAB} + P_{DDAB,m}D_{mic} \quad (3.11)$$

where D_{DDAB} and D_{mic} are the diffusivities of DDAB in LC, resembling those in the sample Mx13, and of the DDAB molecules diffusing as the micellar units, respectively. If D_{mic} is associated with the diffusivity of the micelles as single units (diffusing intact), then, according to the Einstein-Stokes relation, one would expect D_{mic} notably lower than D_{DDAB} . Hence, $D_{DDAB,eff}$ should appear lower than D_{DDAB} , which is not supported by the experimental results for $T > T_{IN}$. On the other hand, $D_{DDAB,eff}$ can be approached by D_{DDAB} if $P_{DDAB,m} \ll P_{DDAB,LC}$. This as well turns out to be not reasonable because this would question the formation and the integrity of the micelles, occurrence of which has been proven by a number of other experimental techniques [13]. Thus, the experimental results shown in Figure 3.16 necessitate, quite generally, that $P_{DDAB,LC}D_{DDAB} \approx P_{DDAB,m}D_{mic}$. This condition can only be valid if, on the time scale of the retention time of the surfactant molecules in the micelles, they can displace by distances yielding sufficiently high values of D_{mic} . This provisionally can be provided if the surfactant molecules in the micellar shells are highly mobile and the retention time is such that the molecules displace by the distances comparable to micellar sizes before they leave the micelle. It is interesting to note in this respect that when the density of the micellar phase in LC in the sample MD15 increases at $T < T_{IN}$ due to the phase separation, the diffusivities of DDAB become slightly higher than those in the sample Mx13. This turns out to be in line with the scenario anticipated in the preceding paragraph.

The second experimental observation reveals a stronger hindering effect of the homogeneously distributed individual DDAB molecules upon translational mobility of 5CB as compared to the effect of DDAB self-assembled into the micelles. Thus, the hypothesis made earlier about the lowering of the 5CB diffusivities in the LC-microemulsion mixture with respect to the pure LC caused by the microemulsion was incorrect. It turns out that dispersed DDAB molecules have larger impact on the diffusivity of LC. Following discussion in the preceding paragraphs, in the LC-microemulsion mixtures DDAB molecules are found both in the micellar and

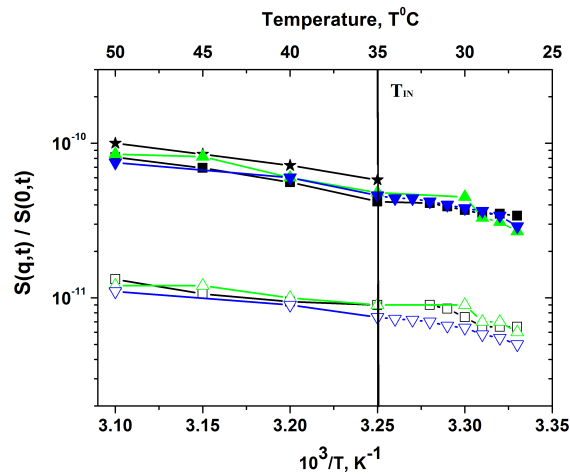


FIGURE 3.17: Arrhenius plot of the diffusivities of 5CB (filled symbols) and of DDAB (open symbols) in MD15 (squares), MD6 (up triangles), and MH8 (down triangles). The data for the diffusivities of 5CB in bulk are shown for comparison by stars.

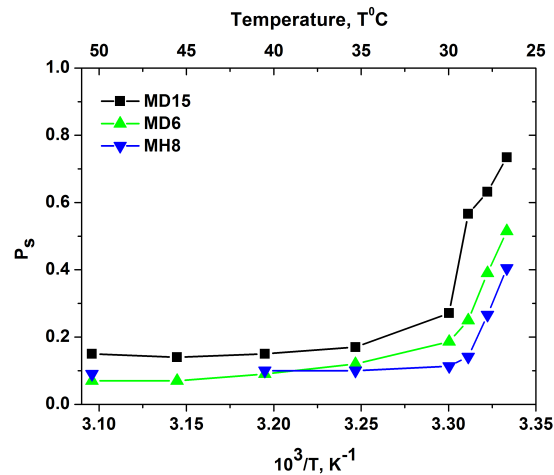


FIGURE 3.18: The fraction P_s of the surfactant component as a function of temperature for the whole temperature range measured.

in the LC phases. The relative fraction of them in the LC phase is lower than in MD13. It is therefore the diffusivities of 5CB in the samples MD15, MD6 and MH8 are found to be between those in the pure LC and in Mx13 as it shown in Figure 3.17. Corresponding populations for surfactant are shown in Figure 3.18. As one may see from the comparison with the data of Table 3.2, the fraction P_s coincides with the calculated proton fractions before the phase separation has started. Therefore, the assumption about the discernibility of both components in NMR experiments is additionally justified and all fits applied to the experimental data are reasonable.

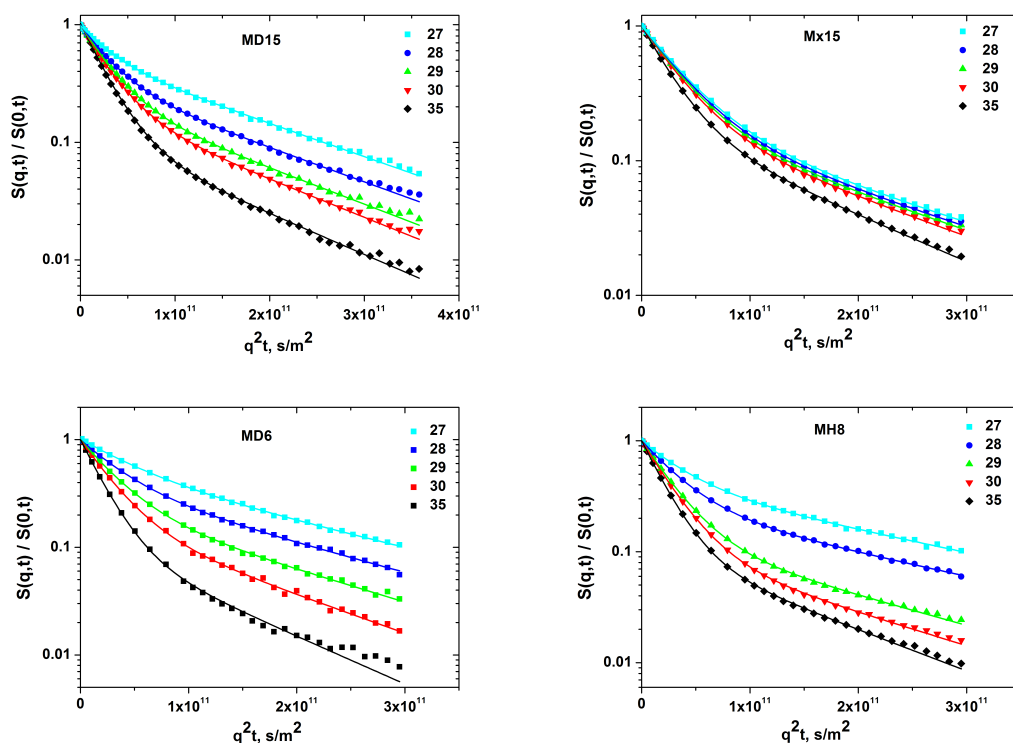


FIGURE 3.19: Normalized spin-echo diffusion attenuations for all samples under study at the same temperatures. The lines are fits obtained using (3.9).

Figure 3.19 summarizes all results obtained by applying the two-exponential fit to the experimental data for the samples under study for the same temperatures. It demonstrates the similar character of the evolution of the echo attenuation curves obtained for all samples having water in their compositions, i.e. the samples, which undergo the phase separation. The phase separation in the sample Mx13 did not occur.

Figure 3.20 shows the diffusivities in linear coordinates for both surfactant and LC components in all samples under investigation starting from the temperature after the isotropic-nematic transition has occurred. Figure 3.20c shows the population of the slow (micellar) component in the same temperature range. One may note, that the data points are rather scattered. Since the population of all phases contributing to the NMR signal cannot be independently identified, the determination of the diffusion coefficients obtained is ambiguous. It is, therefore, we confine ourselves at this stage from making any definitive conclusions on the fine details in diffusion properties before and after phase separation. We only may state that they do not differ notably.

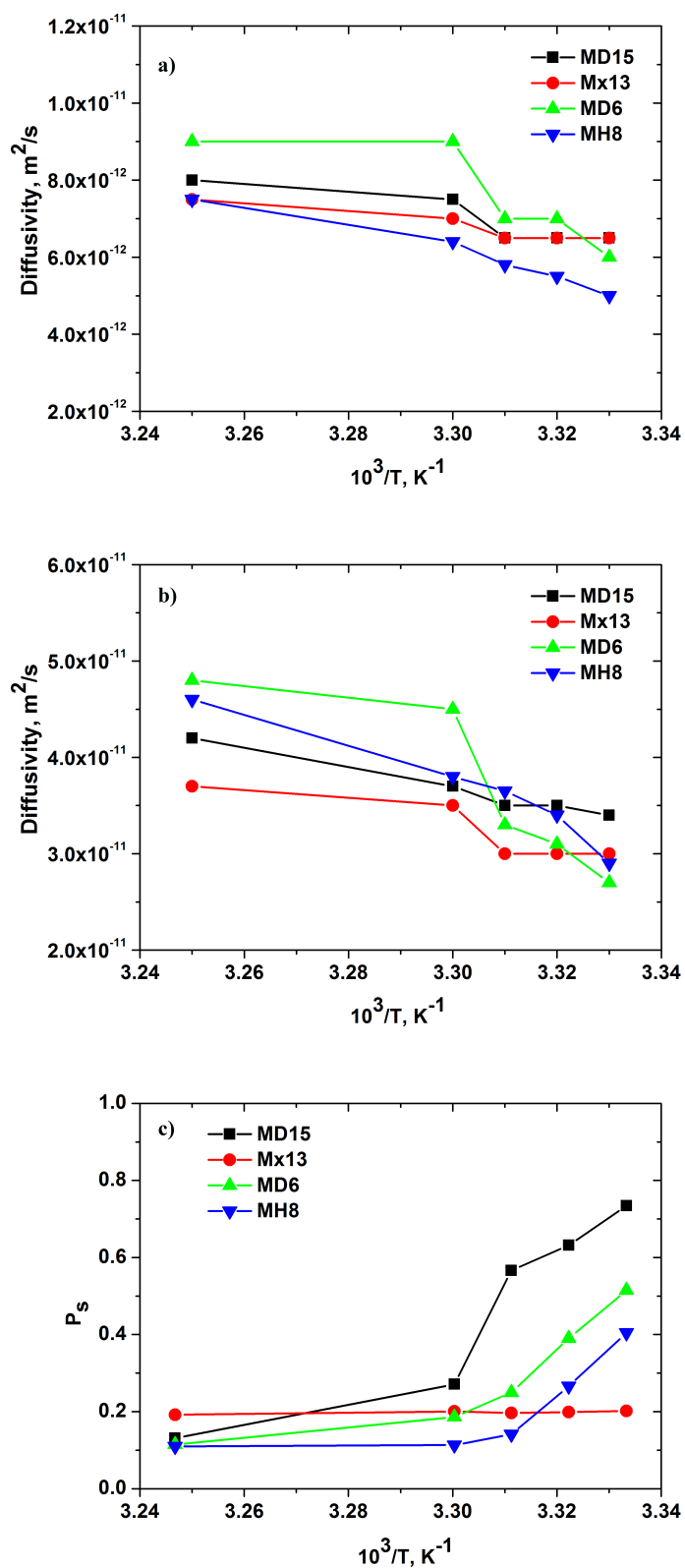


FIGURE 3.20: Diffusion coefficients for the slow and fast components of all samples after the isotropic-nematic transition as a function of temperature (3.20a and 3.20b). The fraction of the surfactant component as a function of temperature is given (3.20c) for comparison.

To conclude this chapter, 1H pulsed field gradient NMR has been applied to study diffusion properties of liquid crystal-microemulsion mixtures. The microemulsions were nano-sized inverse micelles, which were formed upon mixing of water and a surfactant in a thermotropic liquid crystal. Due to an almost one order of magnitude difference in the diffusivities of the liquid crystal and the surfactant molecules, their diffusivities could be with high accuracy probed separately by applying a two-phase model to the measured spin-echo diffusion attenuation functions. The experiments were performed in a temperature range around the isotropic-nematic transition temperature T_{IN} of the liquid crystal.

In the temperature interval above T_{IN} , the diffusivities of the liquid crystal and surfactant molecules were found to follow closely an Arrhenius law $D \propto D_0 e^{-E_A/kT}$ with the activation energy for diffusion of about 31 kJ/mol. With the onset of the formation of the nematic phase at T_{IN} some minor alterations of the temperature dependency are noted. These changes are shown to correlate with the occurrence of the macroscopic phase separation in the system, when the mixture separates into two phases with a very low and relatively high concentration of the micelles in the liquid crystal. Under this condition, the temperature dependency in the whole T range becomes determined not only by varying thermal energy, but also by structural transformations occurring in the samples. No specific features were observed upon approaching T_{IN} from higher temperatures, shining no additional lights on the possible formation of the transparent nematic phase. This may, however, be related to the fact that, with NMR technique, the microscopic dynamics of individual molecules is probed and not of the micelles.

This is found to be in contrast to the system, in which the formation of the micelles was intentionally prohibited by adding to the liquid crystal only surfactant and no water. In this case, no macroscopic separation was observed, rendering thus the phenomenon to be intimately related to the occurrence of the nano-colloids. On considering the diffusion properties of the liquid crystal-surfactant mixture, one of the most important observations was that the diffusivities of the surfactant molecules remained almost unchanged as compared to those in the liquid-crystal microemulsion for temperature above the isotropic-nematic transition temperature. Notably, in the former case, the surfactant molecules diffuse as individual species, while, in the latter case, at least some fractions of time the surfactant molecules should diffuse as a part of the micelles. This finding can be rationalized either by assuming that the micelles diffuse as fast as the surfactant molecules, which certainly contradicts the predictions of the Stokes-Einstein relation concerning different hydrodynamic radii of the two species, or by assuming that on

the time scale of the experiments above 1 ms the surfactant molecules are exchanged between many micelles. In the latter scenario, the renewal time of the micelles turns out to be notably shorter than the experimental time. Because no macroscopic separation occurs for the liquid crystal-surfactant mixtures, the temperature dependency of the diffusivity is found to be smooth in the whole temperature range studied, i.e. no peculiarities are noted for temperatures below T_{IN} .

3.3 Ionic Liquids under Confinement

3.3.1 Ionic Liquids and Confinement Medium

Ionic liquids (IL) are salts with melting temperatures below 100 °C. Due to the vast variability in structure and physicochemical characteristics, they attracted a lot of interest as promising materials in many industrial applications [67, 68]. For instance, they show good solubility and electrolytic properties. Combining different building blocks of IL, i.e. cations and anions, one can tune their characteristics to obtain the desired properties. From this point of view, tuning such parameters as melting point could present high interest for potential applications of IL as solid electrolytes or for improving the material quality [67]. Besides that, we aimed at probing their internal dynamics, namely, how it changes upon varying temperature and confinement conditions. Moreover, following the behavior of ionic liquids under the confinement, we could shed light on the internal structure of confining material. So far, the melting processes of IL under confinement have been rarely addressed. One of such studies was the work by Schulz [7], who used 1-Butyl-2,3-dimethylimidazolium trifluoromethanesulfonate ($B_{2,3}$) as a probe liquid for NMR cryoporometry and concluded about a very high sensitivity of the transition point to the confinement size. Thus, this particular liquid adsorbed in a porous glass has shown a large shift of the melting point. Presuming that large depression of the melting point is determined by the internal structure of an ionic liquid, we have addressed this phenomenon by using three different IL with the only slight difference in their building units (Figure 3.21-3.24). All of them had the same anion, and the difference was only in the number of functional groups (CH_3) and the length of the aliphatic chain in the cations. Importantly, using NMR, we are able to follow the dynamics of cations and anions separately, because the whole measurement cycle can be accomplished on fluorine atoms, composing anions, as well as on hydrogen atoms, which are included in cations.

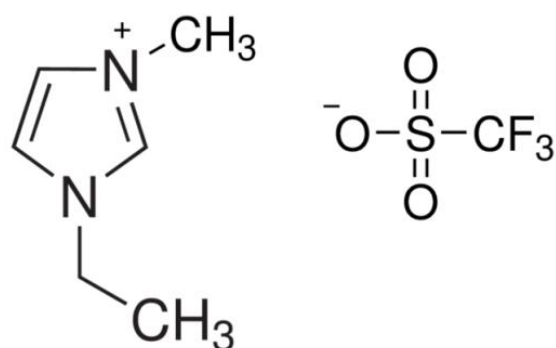


FIGURE 3.21: 1-Ethyl-3-methylimidazolium trifluoromethanesulfonate (1E)

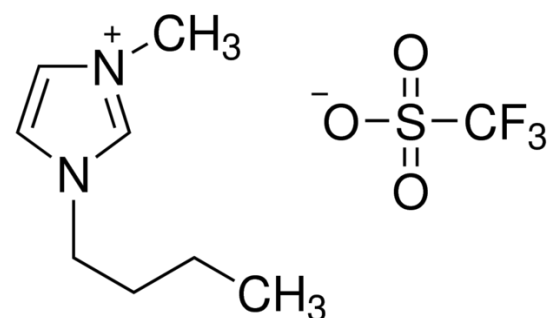
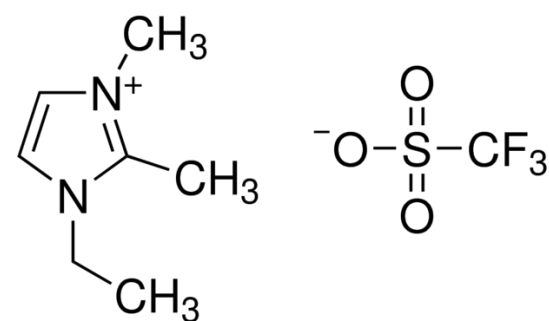
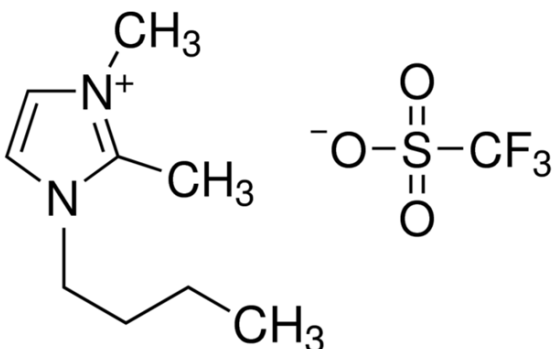


FIGURE 3.22: 1-Butyl-3-methylimidazolium trifluoromethanesulfonate (1B)

FIGURE 3.23: 1-Ethyl-2,3-dimethylimidazolium trifluoromethanesulfonate
($E_{2,3}$)FIGURE 3.24: 1-Butyl-2,3-dimethylimidazolium trifluoromethanesulfonate
($B_{2,3}$)

To investigate the properties of the ionic liquids under confinement, it was essential to find proper porous materials, which could represent an appropriate confinement medium, and structural properties of which could be assessed by other characterization methods. Disordered porous glasses have been chosen as suitable materials. They are mechanically and thermally stable.

In particular, porous glasses (PG) "Trisopor"TM from VitraBio have been used. According to the specification provided by the manufacturer, they have mean pore sizes 32 nm (PG1), 63 nm (PG2) and 111 nm (PG3). The glass particles have sizes between 200 μm and 250 μm . The second series of samples consisted of two other PG with a similar pore morphology. They have the pore sizes 65 nm (PG4) and 154 nm (PG5). These glasses were synthesized in the group of Prof. Dirk Enke, Department of Chemistry, University of Leipzig.

IL are known to be hygroscopic, i.e. they can adsorb some water from the surrounding environment, which may greatly affect their physico-chemical properties [69]. Therefore, to remove water, we heated our samples to temperatures above 100 °C and pumped them over 12 hours. Then, the porous glasses under study were filled with the ionic liquids without access of air. The amount of IL was such to provide an excess of IL covering the porous glass particles.

The porous glass PG1 used in our experiments has pores sizes small enough to give rise to a substantial confinement effect. At the same time, the pores are sufficiently large to adsorb a significant amount of molecules within one pore, thus excluding effects typical for micropores accommodating only several molecules.

To check the specification provided by the producer and to learn more about the structural properties of the confining medium, a series of additional experiments has been performed. Figure 3.25 shows the nitrogen adsorption isotherm measured at 77 K for the sample PG1. The BJH and BET approaches applied to the isotherm measured have provided the parameters of PG, such as the pore volume and the surface, in the reasonable agreement with those of the supplier. The density functional theory (DFT) approach, assuming cylindrical pores, resulted in a relatively wider Pore Size Distribution (PSD) (see inset in Figure 3.25) in the range between 30-60 nm.

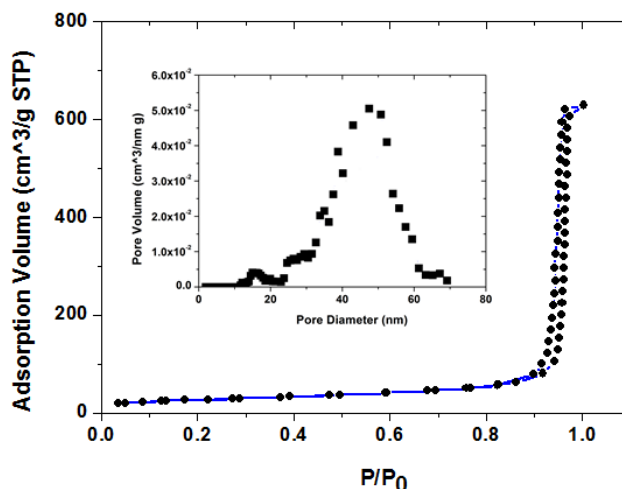


FIGURE 3.25: Nitrogen adsorption isotherm for porous glass PG 1. Inset shows the pore size distribution calculated from the measured isotherm using DFT.

Additional studies of the structural characteristics of the sample PG1 have been performed using NMR cryoporometry. Water and nitrobenzene were used as probe liquids. The Hahn echo pulse sequence was used to record the signal intensity contributed by only liquid phase. After each temperature change, a waiting time of 10 minutes has been given for the system equilibration. The freezing-melting curves obtained reveal hysteresis (Figure 3.26), which is typical for this type of systems.

Indeed, the pore structure of the material under study is expected to be highly disordered. The melting-freezing mechanisms in such glasses are still a matter of discussions. In the part devoted to the NMR cryoporometry, we have discussed some basic scenarios, according which these processes may occur in such systems.

According to [19], it is expected that freezing taken at equilibrium (with corresponding k factor about $100 \text{ K} \times \text{nm}$) and metastable melting (with k factor about $50 \text{ K} \times \text{nm}$) show the so-called neck size distributions, rather than the whole spectrum of the pore sizes. The melting under equilibrium, in turn, may show the large pore sizes, significantly exceeding the neck sizes.

Figure 3.27 contains the patterns discussed above, namely PSD obtained for freezing at equilibrium and PSD for metastable melting, indeed, are found to coincide. The melting branch taken at equilibrium reveals the distribution of the larger pore sizes exceeding the neck sizes by factor of 2. To cross check the data obtained

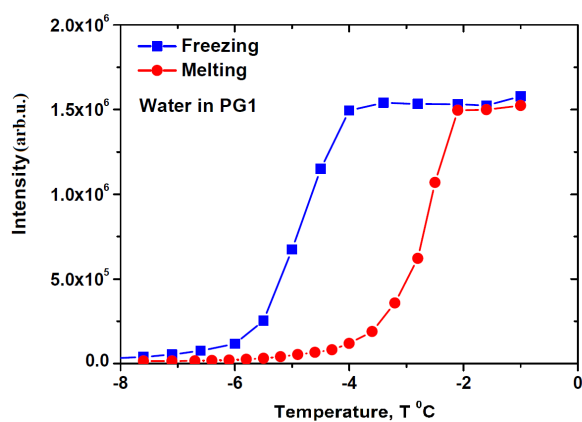


FIGURE 3.26: Freezing and melting curves of water in PG1, showing NMR signal intensity as a function of temperature.

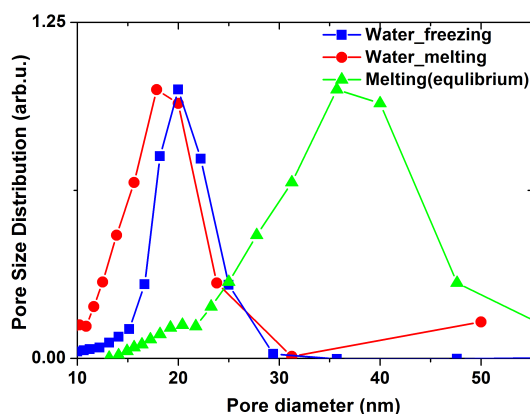


FIGURE 3.27: Pore size distributions obtained using the data of Figure 3.26 by applying Eq. (2.15) to the freezing branch with $k = 100 \text{ K} \times \text{nm}$ and to the melting branch with $k = 50 \text{ K} \times \text{nm}$ and $k = 100 \text{ K} \times \text{nm}$ for metastable melting and melting at equilibrium, respectively.

and, probably, to get some additional information, the similar NMR cryoporometry experiment using nitrobenzene as the probe has been performed. It shows the pronounced hysteresis as well (Figure 3.28).

Considering the melting as equilibrium process, we have found the PSD, which shows the pore sizes even higher (Figure 3.29) than the pore sizes, provided by measurements with water, taking melting in equilibrium.

It is important to mention, that PSD for nitrobenzene was calculated using $k = 250 \text{ K} \times \text{nm}$. However, this value is not obtained by independent measurement of relevant thermodynamical parameters, but it was determined experimentally using porous glasses with different average pore diameters as obtained by gas adsorption

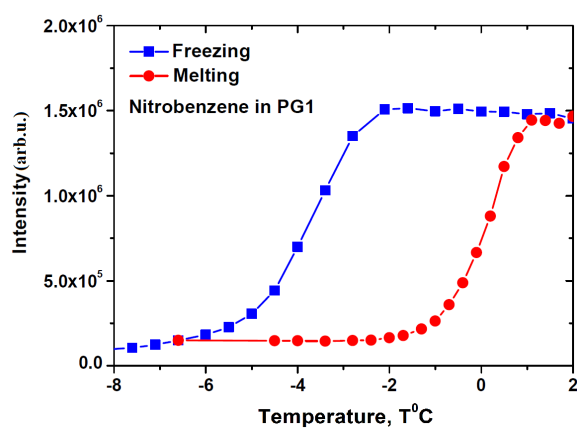


FIGURE 3.28: Freezing and melting curves of nitrobenzene in PG1.

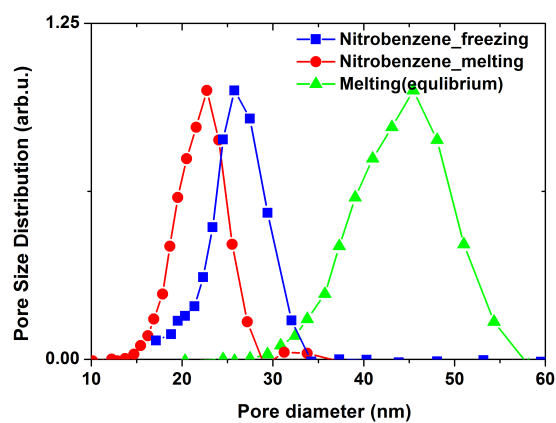


FIGURE 3.29: Pore Size Distributions (PSD) calculated for measured freezing-melting curves of nitrobenzene in PG1.

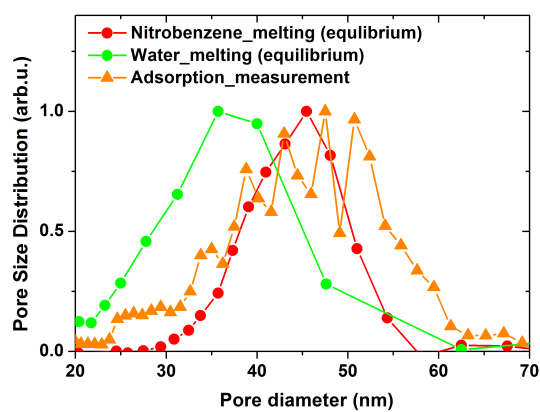


FIGURE 3.30: Summary of PSD of PG obtained using adsorption data and results of cryo measurements with water and nitrobenzene.

experiments. More importantly, that even choosing another k factor the PSD with smaller pore sizes than those, obtained for water, cannot be obtained.

Therefore, combining the data from all three measurements (see Figure 3.30), one may conclude, that the method for characterization of the porous glass used by the producer (32 nm) reveals the low border of pore sizes. The PSD for water in equilibrium was chosen as reliable data for the subsequent analysis.

3.3.2 Melting of Ionic Liquids

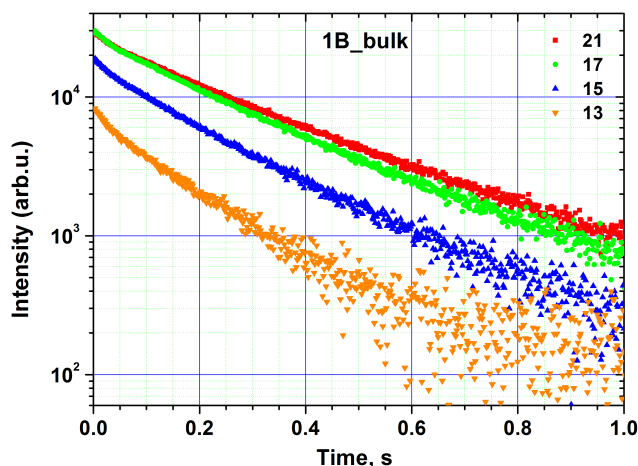


FIGURE 3.31: NMR relaxation curves measured using CPMG pulse sequence for 1B IL in bulk at temperatures covering the melting transition. The intensities are proportional to the amount of IL in the molten state.

The present part is devoted to the NMR study of IL adsorbed in the porous glass considered in the preceding sections. The results of NMR experiments for IL are presented in Figure 3.31. It shows the CPMG curves for bulk 1-Butyl-3-methylimidazolium trifluoromethanesulfonate recorded, given enough time for equilibration after each temperature change. More precisely, they show the dependence of the spin echo intensities measured for different echo formation times. With increasing temperature, there is a transition from low intensities, in almost frozen state, to the higher intensities after melting starts. A relatively strong measurable signal first appears at 13 °C. It grows with temperature increase up to 17 °C. The further increase in T , almost does not change the CPMG curve (see the curve corresponding to 21 °C). The CPMG curves are found to have a multicomponent character. Simple two-exponential fit reasonably fits the data and results in two relaxation times: 20 ms and 200 ms for faster and slower components, respectively.

The two-component relaxation behavior can be caused either by macroscopic heterogeneities (alternating domains containing liquid and crystalline phases) or due to different orientation dynamics of various parts of molecules, giving rise to strong differences in the relaxation rates. To ensure that the IL is homogeneously distributed, namely that there are no regions with substantially different diffusion properties resulting from different states of ILs, and to check how the confinements affect the molecular dynamics, the diffusion measurements have been performed

(see the section Diffusion of Ionic Liquids further). These studies have proven that there is no inhomogeneous distribution of ILs along the sample.

Therefore, the variation of the intensities measured, indeed, reflects the phase state of the whole IL sample at a given temperature, i.e. the degree of melting. Thus, the multiexponential character (Figure 3.31) of the relaxation curves was attributed to different local orientational mobilities of different parts of complex IL molecules. However, the choice of the particular intensity (at zero echo time and at a selected echo time) providing most full information on the phase state is still unclear.

The relevant data, including the data obtained using Hahn echo sequence, are presented in Figure 3.32. One may see, that for all echo times chosen, the intensities plots follow the same master curve. To note, unlike melting of most organic liquids, which have a well-defined transition temperature, IL appeared to have a quite broad region of melting. It does not occur in one sharp step but covers a certain temperature range. Obviously, such behavior imposes additional difficulties for the data analysis. Because there is no pronounced difference between the data of Figure 3.32, we use in what follows the zero-time intensities, I_0 , as a degree of melting.

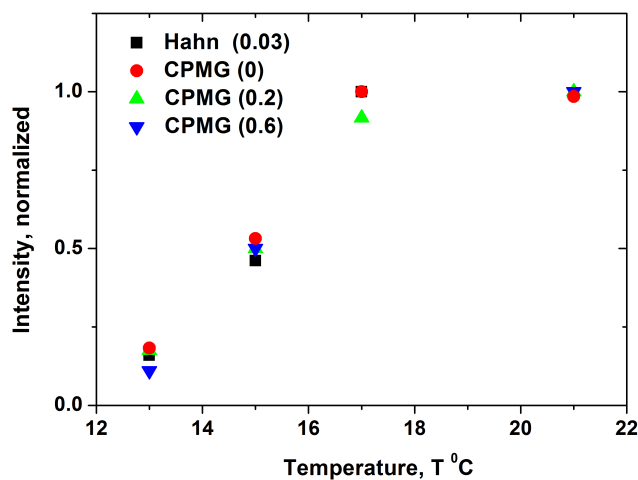


FIGURE 3.32: Comparison of the spin-echo obtained intensities using Hahn ($\tau = 30$ ms) and CPMG sequences. The intensities were taken from CPMG curves in Figure 3.31 at different times, 0.2 s, 0.6 s and extrapolated to 0 s.

During the next step, the same measurement procedure was repeated for IL under the confinement. Figure 3.33 shows the results of CPMG measurement for 1-Butyl-3-methylimidazolium trifluoromethanesulfonate adsorbed in PG1.

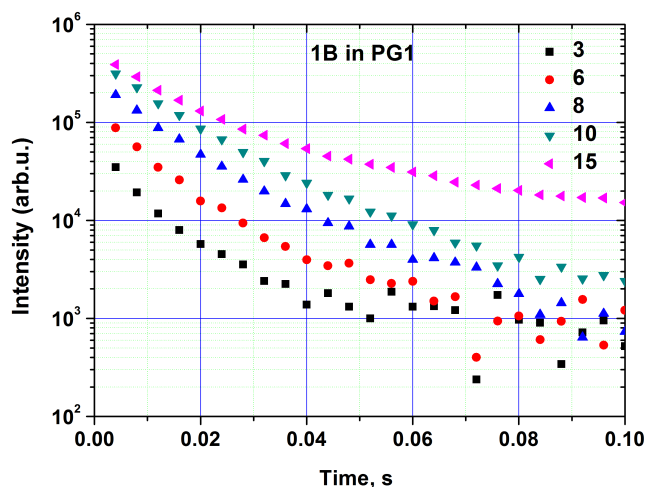


FIGURE 3.33: CPMG curves for 1B IL in PG1 at temperatures covering the melting transition.

Firstly, the confinement leads to the large change in the melting temperatures. A relatively strong measurable signal appears already at 3 °C. It grows with temperature increase up to 10 °C. The further temperature increase give rise to melting in the bulk phase (the sample has an excess of bulk) as it shown by the curve at 15 °C. Moreover, the slower components (with relaxation time 200 ms) in CPMG curve for IL in the pores are found to be dramatically shortened. It is also clear from the comparison with the curve recorded at 15 °C, corresponding to the melting of the bulk phase. The observed shortening in relaxation times could be associated with a stronger effect of confinement on the local dynamics of certain parts of the IL molecules. More importantly, the character of melting remained the same, namely it does not occur in one sharp step but covers a certain temperature range. In what follows, I_0 (the intensities obtained from CPMG curves by extrapolating to zero), were used further as a value representing a degree of melting.

3.3.3 NMR Cryoporometry using Ionic Liquids

The melting curves obtained using the intensities I_0 of Figure 3.33 are shown in Figure 3.34. One of the curves is for 1-Butyl-3-methylimidazolium trifluoromethanesulfonate in the bulk state, which shows the complete melting at approximately 17 °C. This is found to be in a good agreement with the literature data. The second melting curve is for IL adsorbed in PG1. It shows a very large shift of the melting temperature towards lower temperatures. Thus, already at 3 °C the measurable signal appears. That means that melting starts approximately at this T . Upon increasing temperature further, the signal growth ends at ~ 10 °C, i.e. does not change significantly with the further T increase. The full melting in the pores occurs thus to 10 °C. A further small increase in the intensity corresponds to the onset of melting of the bulk phase (the sample had an excess of the bulk phase). Therefore, the melting temperature range is significantly shifted towards lower temperatures in comparison to bulk. Since the parameters of PG1 are already known, it is easy to define the k factor, by matching the PSDs obtained for water using Eq. (2.16) and the pore size distribution for the same material, using the ionic liquids (see Figure 3.35).

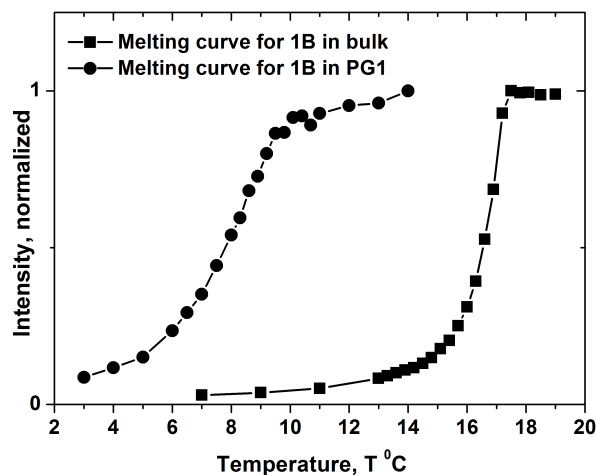


FIGURE 3.34: CPMG experiment on PG1 using 1B IL. The normalized intensities of CPMG signal for bulk IL and IL in PG1.

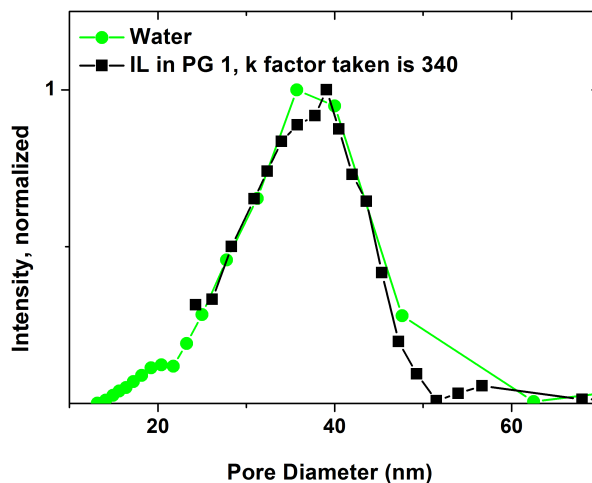


FIGURE 3.35: PSD of water and 1B in PG1, taking k factor as $340 \text{ K} \times \text{nm}$

Using the data of Figure 3.34 and Eq. (2.14) together with Eq. (2.15) we could find the k factor for the IL considered. The k factor thus obtained results to be relatively large, $k \approx 340 \text{ K} \times \text{nm}$). This is close to that obtained by Schulz for another ionic liquid [7]. The large value of k makes 1-Butyl-3-methylimidazolium trifluoromethanesulfonate a good probe liquid for NMR cryoporometry. With the known k factor, this IL can be applied as a probe liquid providing a very high spatial resolution to other porous materials. As a result, to prove the above-described conclusion, we continued NMR measurements on other porous glasses: two additional PG provided by VitraBio, PG2 (63 nm) and PG3 (110 nm), and PG produced in the Department of Chemistry of Leipzig University by group of Prof. Dirk Enke, PG4 (65 nm) and PG5 (154 nm). The respective melting curves are shown in Figure 3.36.

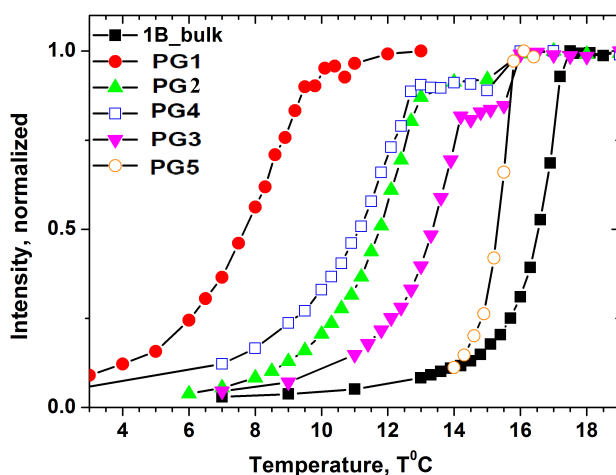


FIGURE 3.36: Melting curves for 1B in all porous samples used in the experiments.

As the next step, using k factor obtained, we could calculate the respective pore size distributions (Figure 3.37 and Figure 3.38). The results are presented separately to make all details more visible. To recall, they have been calculated assuming an equilibrium character of the melting transition, i.e. they show the higher mode of the real PSD.

For the VitraBio porous glasses with the pore size 63 nm (PG2), according to the manufacturer, slightly higher pore sizes were obtained in our experiments (Figure 3.37). The porous glass with the declared pore size 110 nm (PG3) has shown a very wide PSD with an undefined peak in the range between 60 nm and 100 nm, thus giving, in contrast to the previous one, the lower mode of the real PSD.

The results on a second series of PG provided by group of Prof. Enke are presented in Figure 3.38. The declared pore sizes were defined by liquid nitrogen adsorption measurements. The porous glass PG4 with pore sizes 65 nm revealed a good consistence with our data. The porous glass PG5 with pore sizes 154 nm shows again the higher mode of the real PSD.

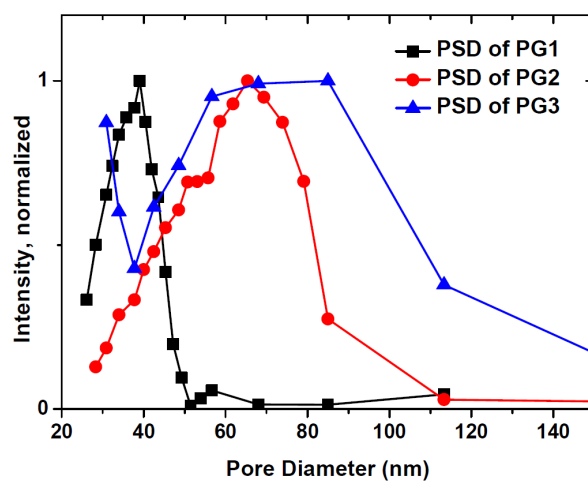


FIGURE 3.37: PSD calculated for VitraBio porous glasses.

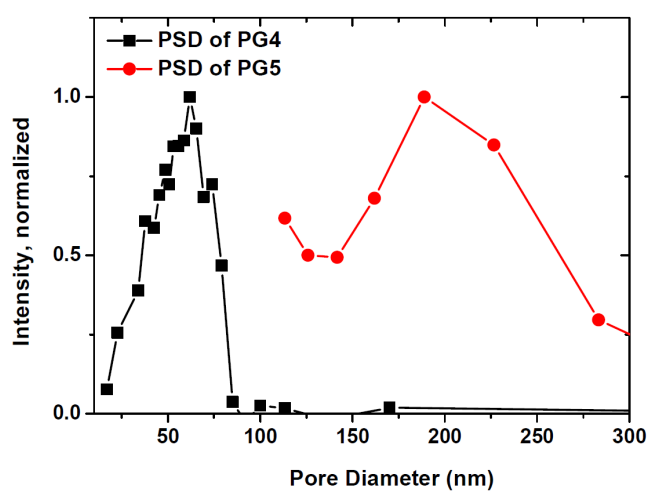


FIGURE 3.38: PSDs calculated for the porous glasses provided by group of Prof. Enke.

3.3.4 Diffusion of Ionic Liquids

In this section, we present the results of diffusion measurement for ionic liquids under investigation. Since cations have hydrogen atoms and anions have fluorine atoms, their diffusion dynamics could be followed using the effect of nuclear magnetic resonance on hydrogen and fluorine, respectively. Figure 3.39 shows the spin-echo diffusion attenuation curves for 1B in bulk and adsorbed in PG1 measured for cations and anions separately. The slope of the lines defines the diffusivities (see the part devoted to PFG NMR). As revealed by the data, cations diffuse faster than anions. This is in a good agreement with the literature data for similar systems [69]. Also, as it was expected, molecules in bulk diffuse faster than under confinement [70]. The curves presented in Figure 3.39 are of a mono-exponential shape, including for adsorbed IL in PG1. Therefore, the homogeneous distribution of IL inside the samples is ensured.

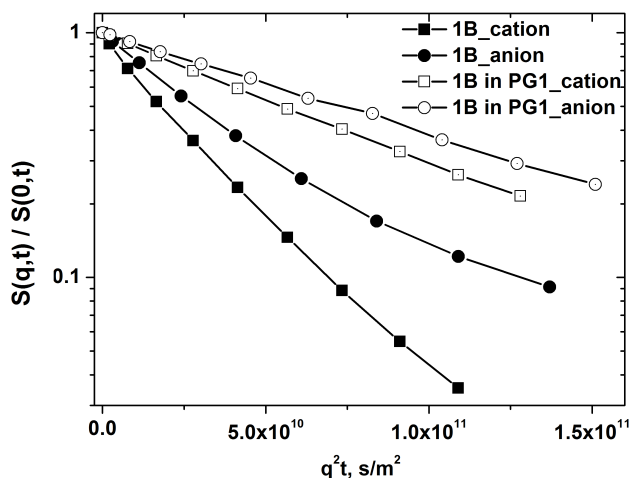


FIGURE 3.39: Diffusion attenuation curves for 1B in bulk and adsorbed in PG1 measured for cations (NMR on hydrogen atoms) and anions (fluorine atoms). Solid symbols correspond to bulk, empty ones to IL inside the porous glass.

The diffusion coefficients obtained by the simple mono-exponential fit using data of Figure 3.39 are presented in Table 3.3.

1B cation	$(3.5 \pm 0.1) * 10^{-11} m^2 s^{-1}$
1B anion	$(2.4 \pm 0.1) * 10^{-11} m^2 s^{-1}$
1B cation in pores	$(1.2 \pm 0.1) * 10^{-11} m^2 s^{-1}$
1B anion in pores	$(0.95 \pm 0.05) * 10^{-11} m^2 s^{-1}$

TABLE 3.3: Diffusion coefficients for 1B in bulk and adsorbed in PG1 for cation and anion correspondingly.

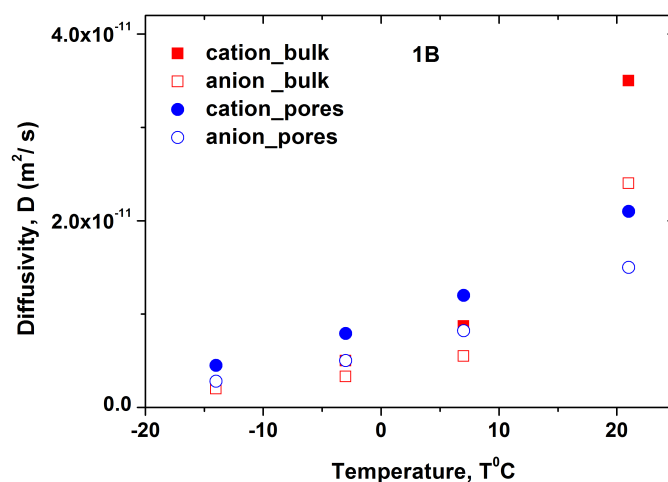


FIGURE 3.40: Diffusivities for 1B in bulk and adsorbed in PG1 measured for cations (hydrogen atoms) and anions (fluorine atoms). Solid symbols show cations, empty ones anions.

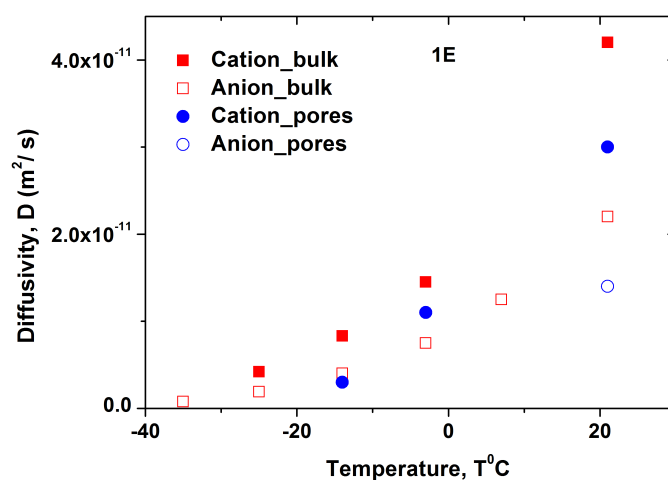


FIGURE 3.41: Diffusivities for 1E in bulk and adsorbed in PG1 measured for cations (NMR on hydrogen atoms) and anions (fluorine atoms). Solid symbols correspond to cations, empty ones to anions.

To get some additional information, the possibility to measure the diffusion coefficients both for cation and anion during the cryo NMR experiment was exploited. Figure 3.40-3.41 show the diffusivities for 1-Butyl-3-methylimidazolium trifluoromethanesulfonate and 1-Ethyl-3-methylimidazolium trifluoromethanesulfonate in broad temperature ranges. The monoexponential character of echo attenuation curve was observed in every single measurement for both IL considered, thus confirming the homogeneous distribution of IL adsorbed in the porous glass.

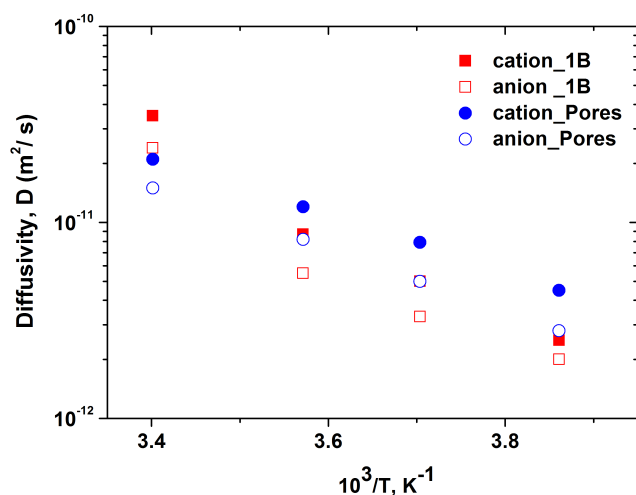


FIGURE 3.42: Arrhenius dependence of diffusivities for cations and anions of 1B in bulk and adsorbed in PG1.

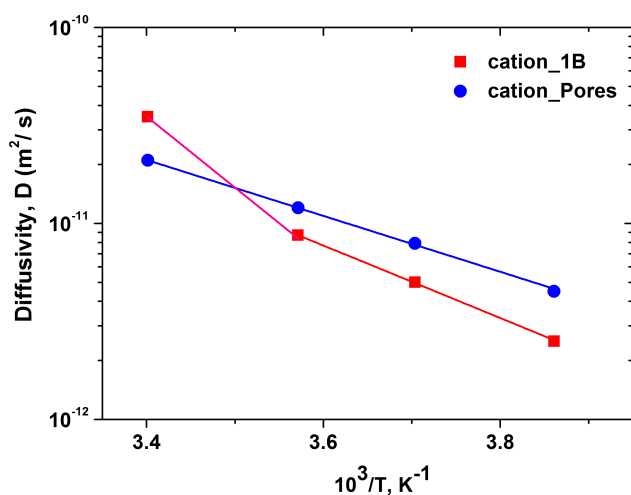


FIGURE 3.43: Arrhenius dependence of diffusivities for cations only. The lines show the fit of the Arrhenius equation to the data. Their slope gives the activation energies.

As the next step, we plot the diffusivities in the Arrhenius coordinates (Figure 3.42). To simplify the picture, we leave only the data for cations (Figure 3.43). The same analysis is valid for anions as well.

One may see that the character of the plots is different in for bulk IL and IL adsorbed in pores. The activation energy, E_A , for 1B adsorbed is about 27 kJ/mol. In the case of bulk IL, the situation is more complicated. It could be directly related to the confinement effect. Because of the phase transition (from the frozen

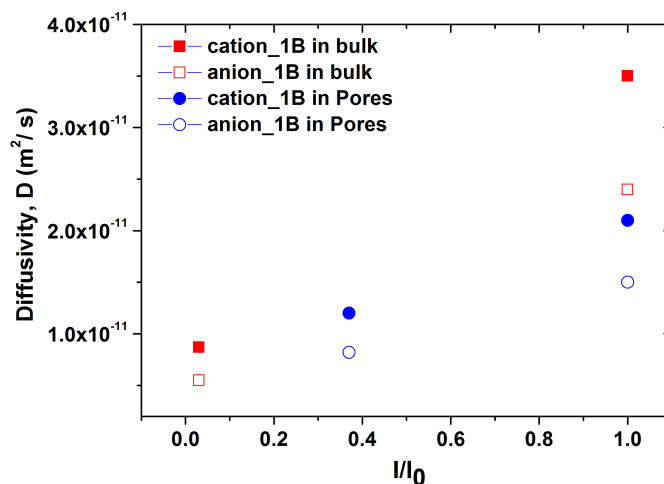


FIGURE 3.44: Diffusion coefficient as a function of the NMR signal intensity measured.

to the molten state), there are two regions with different activation energies equal 35 kJ/mol and 69 kJ/mol.

One of the remarkable results revealed by Figures 3.42-3.43 is the fact that, in a certain temperature range, the diffusivity in the pore spaces is even faster than in bulk. To analyze this, the dependence of the diffusivities on the NMR signal intensity at the same temperatures was compiled. The data are shown in Figure 3.44, which includes diffusivities of cations and anions in bulk and in adsorbed IL only for temperatures: 7 °C (4 points in the left part of the Figure 3.44) and 21 °C temperature (4 points in the right part of the Figure 3.44). At 7 °C, the NMR signal intensities for cations and anions in pores are found to be larger than those for bulk. Therefore, at the same temperature, the degree of melting for IL under confinement is higher. In the case of bulk IL, the melting at that temperature only starts, and we are dealing with the situation when only some parts of IL molecules become mobile, what results in the substantially lower diffusion coefficients. At the room temperature (21 °C), when IL is molten completely, the diffusion coefficients in bulk are higher than those in pores, giving the tortuosity factor of about 1.5. It is also consistent with the literature data for the porous glass considered.

3.3.5 Correlations between the Structure and Properties of Ionic Liquids

One of the goals of this work was to explore the effects of the chemical structure of IL on their melting points. In what follows, we present the similar study, but using another IL, namely 1-Ethyl-3-methylimidazolium trifluoromethanesulfonate with a shorter aliphatic chain (see Figure 3.24).

The peculiar properties revealed for 1B, namely the multicomponent relaxation curves and the melting transition occurring over a finite temperature interval are also found to be true for 1E. The k factor is found to be slightly smaller (about $250 \text{ K} \times \text{nm}$). The next ionic liquid, 1-Ethyl-2,3-dimethylimidazolium trifluoromethanesulfonate (E_{23}) has shown a very high melting point (above 100°C). Since high temperatures can imply the additional difficulties on the NMR cryoporometry experiment, we did not investigate this liquid further. Both ionic liquids measured in our experiments (1B and 1E) in comparison to the results of Schulz [7] for the ionic liquid B_{23} (note that all these three experiments have been performed using one and the same porous material PG1) are shown in Figure 3.45.

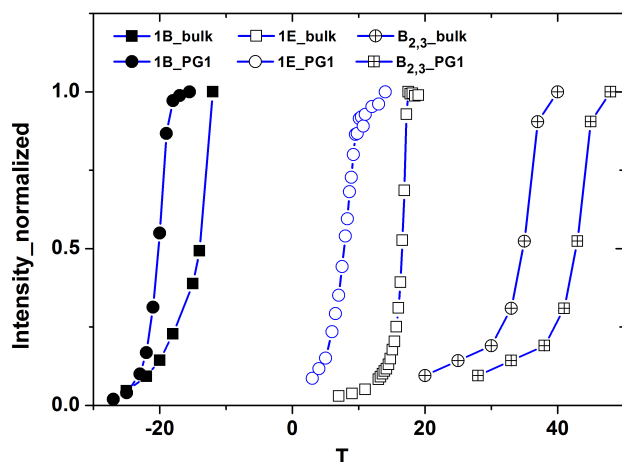


FIGURE 3.45: Melting curves for 1B, 1E, B_{23} in bulk and adsorbed in PG1.

Based on these results, the following conclusions may be drawn:

Firstly, the longer aliphatic chain lengths of cations in 1B and B_{23} (see Figures 3.21-3.24) result in higher k factors than those for 1E with shorter aliphatic chain lengths. Recall that higher k factor means larger suppression of the melting point as compared to the equilibrium transition point in bulk substances. Therefore, one may assume that increasing of the aliphatic chain length may lead to the increase

of the k factor. Secondly, for IL 1B and B_{23} the longer chain length also leads to the higher melting T in comparison to 1E. But this pattern is ruled out in the case of $E_{2,3}$, where the chain length is the same as in case of 1E, but the melting T significantly exceeds those for all other IL considered. However, it could also be determined by one extra functional group (CH_3) in $E_{2,3}$. At the same time, despite of the different number of functional groups and the aliphatic chain lengths, the ionic liquids under study revealed the same character of the freezing-melting processes. Diffusion measurements for two IL (1E and 1B) have also not shown any detectable effect of this subtle chemical structure on the dynamical behavior.

We assume that the aforementioned structural-dynamical dependencies exist. Nevertheless, they could be reliably established by using a broader range of IL. The more precise measurements should be applied. This is the aim for our future studies.

3.4 Diffusion in Nanoporous Glasses

3.4.1 Porous Glasses Obtained by Spinodal Decomposition

Favorable properties of mesoporous materials, including among others, high surface area, low transport resistances, and easy handling of macroscopic shape, determine an increasing interests for their use in practical applications [71, 72]. Nowadays, they are widely used for mass separation, catalysis, drug delivery, etc. To provide an optimal efficiency of technological processes involving mesoporous solids, their structural properties, such as mesopore size or macroscopic shape, have to be properly adjusted to meet the application-specific requirements. In particular, the pore size distribution and the pore geometry determine the accessibility of the inner surface, the local mobility and long-range transport properties of porous materials. Therefore, the ability to intentionally vary the internal pore structure of mesoporous materials is a challenging task for material scientists. For porous solids obtained via phase separation of the alkali-borosilicate glasses [4], a purposeful design of the pore structure can be based on the variation of the conditions under which the process of the microphase separation takes place.

The basic procedure used in preparation of these porous glasses is so-called spinodal decomposition, which is illustrated in Figure 3.46. Spinodal decomposition is a mechanism of demixing of a mixture of liquids or solids from one thermodynamic phase into two coexisting phases. In our case, a thermal treatment of the initial alkali-borosilicate glasses leads to the above-mentioned process, resulting in two finely dispersed sodium borate-rich and silica-rich phases. This process is mostly controlled by the glass composition. Further growth or evolution of the thus formed regions with different chemical compositions depends on the temperature under which the heat treatment is performed, and a time period given to the system to evolve. This time period will be referred to as treatment time. During this stage, the two phases grow slowly. Upon the subsequent quenching of the system to low temperatures, the evolution can be terminated and the phase-separated domains get spatially arrested. Further leaching with hydrochloric acid can be used to remove the borate-rich phase and leave behind a silica-rich matrix material, forming a network with a three-dimensional, disordered pore system. The pore sizes in thus obtained materials can further be enlarged by a post-treatment.

In this part of work, the option to control the internal mesopore structure of phase separated alkali borosilicate glasses by varying the conditions of microphase

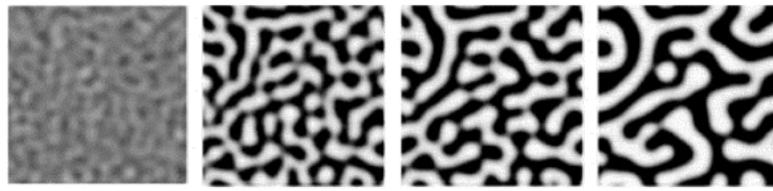


FIGURE 3.46: Spimodal decomposition of borosilicate phase during the preparation of nanoporous glasses

separation has been studied. For this purpose, we have studied how different material properties correlate with the preparation conditions. Structure and transport characterization of a family of nanoporous glasses obtained under different conditions has been performed using a combination of several experimental techniques, including gas adsorption, nuclear magnetic resonance cryoporometry and diffusometry. A series of nanoporous glasses was prepared in Department of Chemistry, Leipzig University, by leaching of phase separated initial glass beads with mean particle diameters between $100 \mu\text{m}$ and $200 \mu\text{m}$. The composition of initial glass was 70 wt % SiO_2 , 23 wt % B_2O_3 and 7 wt % Na_2O . The glass beads of spherical shape have been used to resist high heating/cooling rates and to avoid the uncontrolled phase separation during the cooling and shaping processes. The temperatures and durations of the heat treatment for porous glasses are given in Table 3.4. In addition, two samples were leached with 0.5 N NaOH after synthesis for two 2 h. These samples are marked by asterisks. Further details on the NPG synthesis can be found in [4].

Sample	Temperature [K]	Treatment time [h]
PG-540-4	540	4
PG-540-10	540	10
PG-540-12	540	12
PG-540-14	540	14
PG-540-24	540	24
PG-540-48	540	48
PG-550-48	550	48
PG-540-48*	540	48
PG-550-48*	550	48

TABLE 3.4: Nanoporous glass samples obtained using different temperatures and heat treatment times.

3.4.2 Nitrogen Adsorption Data

The first information about nanoporous glasses have been provided by nitrogen adsorption. The nitrogen adsorption isotherms were measured at 77 K by an automated gas adsorption apparatus (Micromeritics). The sample cell was kept at 77 K by complete immersion into liquid nitrogen. Prior to the adsorption experiments all samples were degassed for at least 10 h at 520 K under vacuum.

Figure 3.47 shows the nitrogen adsorption for three representative samples using different treatment times. For a family of samples from PG-540-10 to PG-540-24, the isotherms appear to be almost identical, and therefore, not all of them are shown. The main feature revealed by Figure 3.47 is that, for the samples obtained using the treatment times of 24 h or less, the desorption behavior is completely controlled by cavitation due to strong pore blocking, namely the larger pores empty at a cavitation pressure P_{cav} corresponding to the limit of mechanical stability of the confined fluid, while leaving the smaller pores filled with the capillary-condensed phase [73]. That means that the majority of the mesopores are connected to the external gas atmosphere through micropores or mesopores with the pore sizes smaller than approximately 5 nm. Increasing the treatment time to 48 h leads to the formation of a continuous mesopore network with the pore sizes exceeding 5 nm, as it is revealed by the shift of the evaporation pressure to higher values. Notably, this mesopore network spans the whole particle from its center to the outer surface. Under the condition of the cavitation-controlled desorption, the pore size analysis is most reliably performed using the adsorption branch of the isotherm.

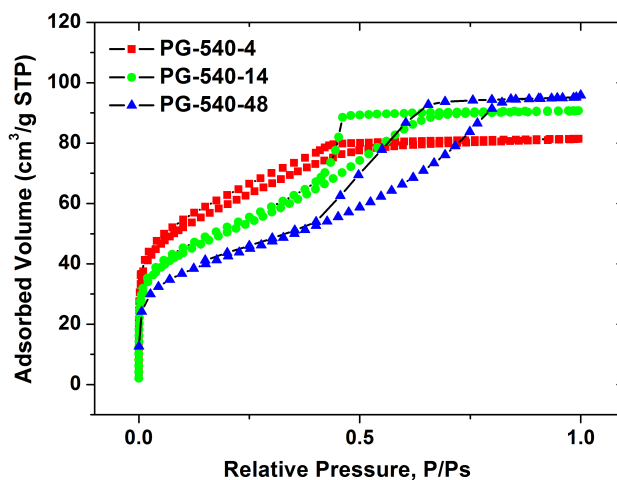


FIGURE 3.47: Nitrogen adsorption isotherms for three representative samples measured at 77 K.

By applying the density functional theory and treating the adsorption branch to be governed by the metastable capillary condensation, the pore size distributions (PSD) for the data of Figure 3.47 resulted as shown in Figure 3.48. The mode of the PSDs associated with the peak around 1 nm can be left out of consideration. In fact, it may result as an artifact of the analysis procedure. For the mode associated with the mesopore sizes above 2 nm, a clear tendency, namely increase of the pore sizes with increasing treatment time, is observed. The average pore size increases from about 3.5 nm for PG-540-4 to 6.5 nm for PG-540-48. At the same time, the distribution width also increases. Thus, if for PG-540-4 all pores are found to be smaller than 5 nm, a broad distribution from 2 to 10 nm is observed for PG-540-48.

Most notably, PSD for PG-540-14 is centered around 5 nm, i.e. this sample contains a substantial amount of small mesopores with the pore sizes below 5 nm. Therefore, as revealed by the data of Figure 3.47, the predominant mechanism responsible for emptying of the pore network is cavitation. As shown in Figure 3.49, with increasing treatment time beyond 14 h the occurrence of a more rounded evaporation transition is observed. This indicates that some part of the pore space is emptied at equilibrium under the pore-blocking control, while evaporation from the rest part is still controlled by the cavitation phenomenon.

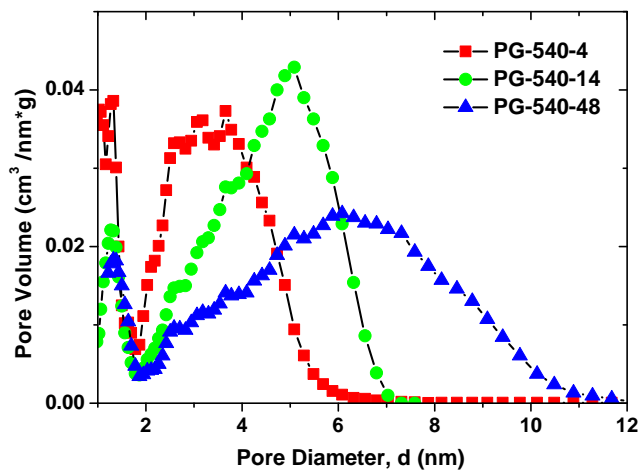


FIGURE 3.48: Pore size distributions obtained from nitrogen adsorption data of Figure 3.47.

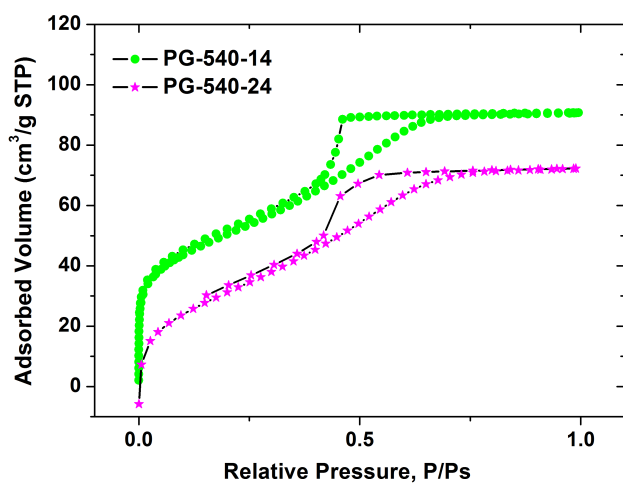


FIGURE 3.49: Nitrogen adsorption isotherms for two samples obtained with the heat treatment times of 14 and 24 h. One of the curves is shifted downwards for better representability.

3.4.3 Results of NMR Cryoporometry Experiments

For the NMR cryoporometry experiments [15, 16], the procedure of the sample preparation described in the section devoted to NMR cryoporometry, was applied.

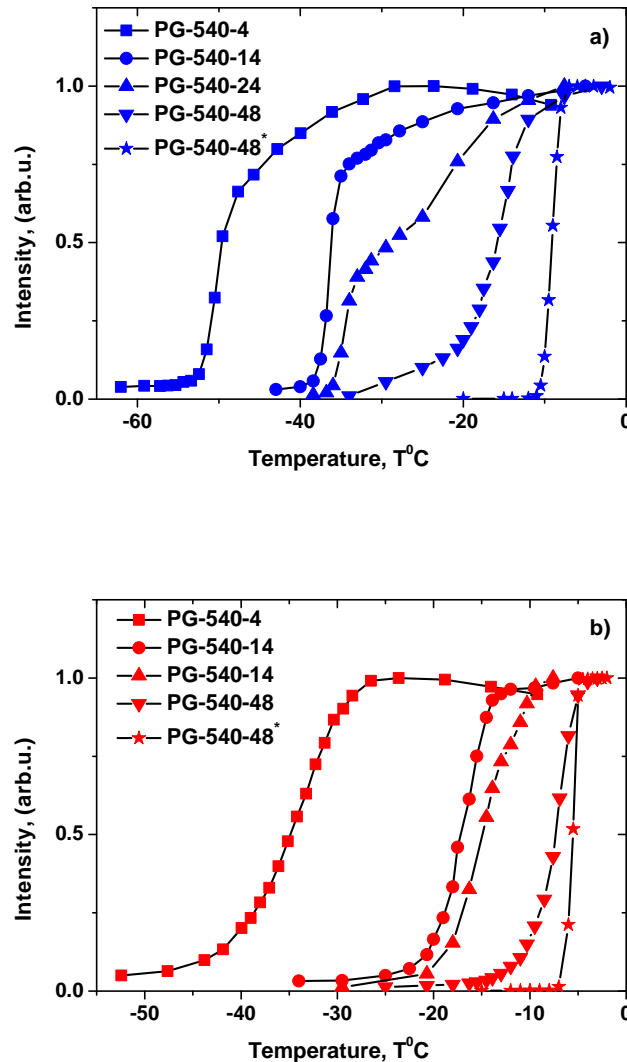


FIGURE 3.50: Fractions of the liquid water phase in pores measured for selected NPG during (a) cooling and (b) warming.

The results of NMR cryoporometry experiments, in which the relative fractions of the liquid phase are measured upon cooling or heating, are shown in Figure 3.50. Only the data points obtained for temperatures below the bulk transition temperature $T_0 = 0\text{ }^{\circ}\text{C}$ are shown. The both freezing and melting transitions in the pore space are found to be strongly suppressed as compared to T_0 . Moreover, they reveal the formation of a pronounced hysteresis between them. The mechanisms responsible for such behavior are, in details, described in the section devoted to

NMR cryoporometry. For the materials studied in this work, which possess relatively narrow PSDs, the dominant mechanism of freezing is the ice-phase invasion. Under these conditions, the analysis of the freezing transition, assuming its equilibrium nature, yields the neck size distribution. On considering water, which has been used as a probe liquid in our experiments, the cryoporometry constant k results as $k_{eq} = 99 \text{ K nm}$, as obtained from the freezing behavior of water in MCM-41 materials with tubular pore geometry [76].

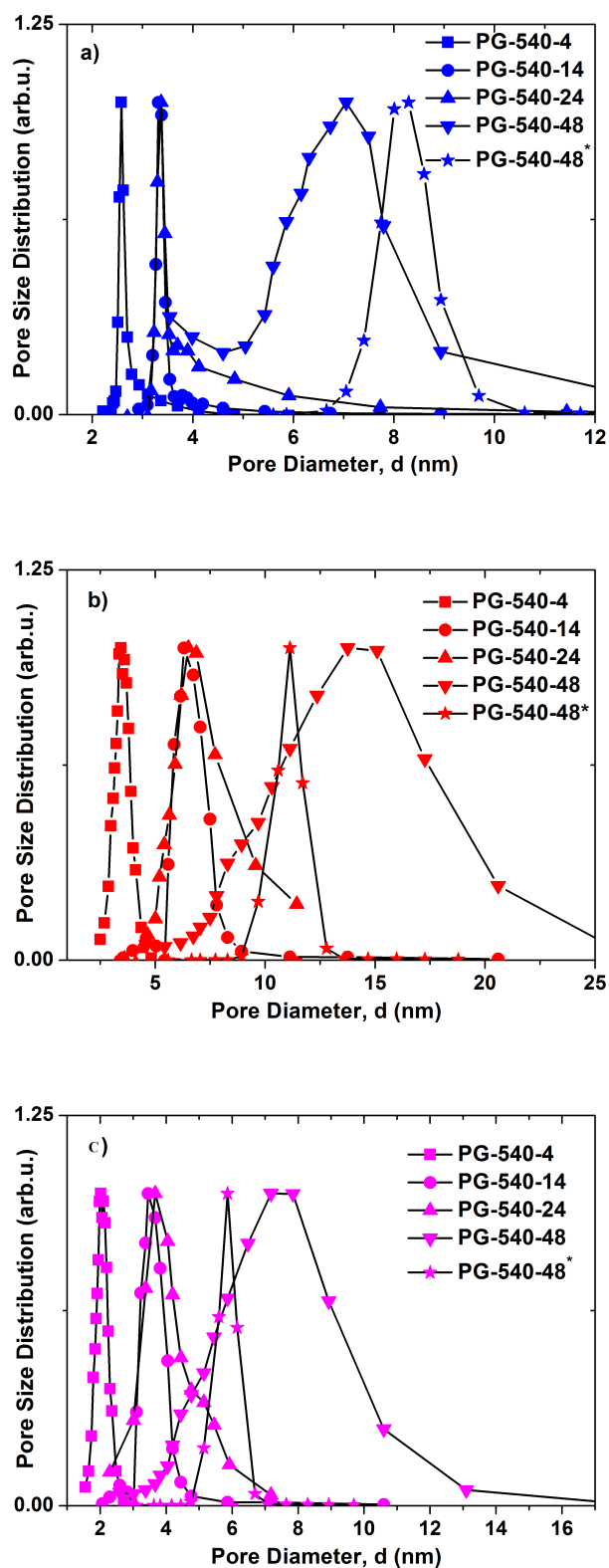


FIGURE 3.51: Pore size distribution calculated from a) the freezing branch, assuming equilibrium freezing, and from the melting branch, assuming b) equilibrium and c) metastable radial melting mechanisms.

On the warming branch, there are several mechanisms contributing to the process of melting in materials with disordered pore structures [19], which are also described in the section devoted to NMR cryoporometry. Correspondingly, the pore size analysis performed assuming the metastable character of the melting transitions yields the distribution of neck sizes. To do this, one shall use the cryoporometry constant k_m associated with radial melting in cylindrical pores. The latter has been shown to result as $k_m = k_{eq}/2$ [17]. In the second case, the pore size analysis performed by using the equilibrium cryoporometry constant k_{eq} may provide a part of the whole PSD associated with the largest pores.

On the basis of these scenarios discussed for the freezing and melting processes, the data of Figure 3.50 can now be easily rationalized. The monotonic decrease of the liquid fraction upon cooling in the sample PG-540-4 from 1.0 to about 0.75 (Figure 3.50a) can be associated with the strong pore-blocking effect due to the existence of a substantial amount of narrow pores prohibiting the ice phase invasion from the outer surface. An abrupt freezing of the entire mesopore space at about -50 °C indicates that the equilibrium transition temperature for the smallest pores is attained at this temperature. This allows the ice phase to percolate throughout the porous particle. PSD obtained from the freezing data of Figure 3.50a by using k_{eq} is shown in Figure 3.51a. The figure reveals the existence of a very narrow neck size distribution centered around 2.7 nm. Upon increasing the treatment time to 14 h (sample PG-540-4), the freezing behavior changes only quantitatively. Like in the previous sample, the majority of the mesopore volume (about 75 %) freezes at one step, but at a higher temperature of -40 °C. The respective PSD is shown in Figure 3.51a. One may, therefore, conclude that, during this stage of the heat treatment, the shape of the mesopore size distribution (at least associated with the smallest pores) does not change, but the average size of small mesopores shifts to higher pore sizes. Thus, according to the data of Figure 3.51a, the average neck size increases to about 3.4 nm.

Further increase of the treatment time to 24 h (sample PG-540-24) leads to notable qualitative changes in the freezing behavior. Namely, a two-step freezing behavior becomes now clearly observable. This pattern results as a combined effect of two processes. First, the pore sizes increase further with increasing treatment time. In parallel, the volume density of the smallest mesopores (acting as bottlenecks for the freezing process) decreases. In particular, such necks in this sample can completely block only about 50% of the mesopore volume. The rest of the mesopore volume is directly accessible from the outer surface via the pathways connecting only large mesopores. As revealed by the data of Figure 3.51a, the neck size distribution

remains, however, almost identical to that of the previous sample. It also does not change for the sample treated for 48 h (sample PG-540-48), but the density of the small mesopores decreases further to an amount which is able to block statistically only about 50% of the mesopore volume. Because the ice phase invasion does occur here under the weak pore blocking condition, the PSD obtained assuming the equilibrium nature of the transition will closely reflect the real one.

The same conclusion is valid for the sample PG-540-48. Notably, this finding is in a reasonable agreement with the message of the nitrogen gas adsorption. As a final remark of this part, it is worth mentioning that, for the samples obtained with the treatment times up to 24 h, only the peaks associated with the neck size distributions (Figure 3.51a) are meaningful. The higher modes of the PSDs do not bear any real structural information. To access the PSDs associated with the larger pores, the melting behavior has to be analyzed. The PSDs obtained from the melting branch by using the metastable (k_m) and equilibrium (k_{eq}) cryoporometry constants are shown in Figures 3.51b and 3.51c, respectively. To recall, the first approach yields the neck size distribution, while the second one may, under favorable conditions, yield the distribution of the PSDs of the largest pores. The neck size distributions of Figure 3.51b for the samples PG-540-4, PG-540-14 and PG-540-24 are found to be in a good agreement with those obtained from the freezing branch. Some minor discrepancies observed may be rationalized by noting the differences in the thicknesses δ of the non-frozen surface layers resulting during cooling and heating. Indeed, the temperature ranges, in which the freezing and melting transition occurs differ considerably. Consequently, δ will also be different in these temperature ranges, and therefore should be taken into account during the data analysis via Eq. (2.14).

If the melting data are analyzed using the metastable cryoporometry constant k_m , the PSDs for the samples PG-540-4, PG-540-14, and PG-540-24 result to be centered about twice of the average neck sizes. This observation tells unequivocally that melting of the intrapore ice is completely controlled by metastable melting of the necks. As far as a neck melts, it initiates melting of the adjacent pores with the larger pore sizes via the equilibrium mechanism. Because $K_{eq} = 2K_m$, this, according to Eq. (2.14), reveals that the whole PSD is located between two extremes, given by the pore size distributions in Figures 3.51b and 3.51c. This finding is as well in a good agreement with the data of nitrogen adsorption shown in Figure 3.48. It turns also out that the equilibrium melting scenario is not applicable for the samples PG-540-48 and PG-540-48*, which contain mostly relatively

large pores. Thus, the intrapore ice will melt closer to T_{mr} , the temperature at which radial melting does occur.

3.4.4 Diffusion Study

As the next stage, the effective diffusivities for cyclohexane at full pore loadings in nanoporous glasses have been measured.

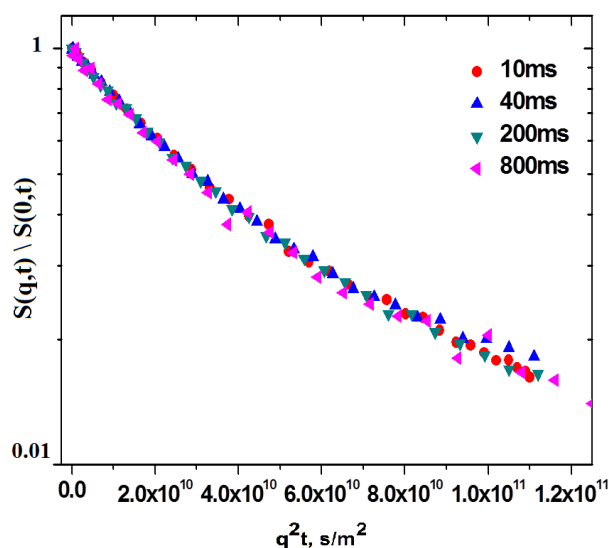


FIGURE 3.52: Normalized spin-echo diffusion attenuations functions at different diffusion times.

For a variety of technical applications, the rates of mass transfer of fluids in porous solids are decisive for the process efficiency [77-79]. In this part of the present work, the transport properties of the nanoporous glasses discussed in the preceding sections are reported and correlated with the structural information obtained. The diffusion studies were performed under two different conditions of (i) full loadings of the mesopore space by the liquid, and (ii) partial pore fillings. In the latter case, the results obtained have a twofold importance. First of all, they demonstrate an option for the variation of the transport properties by changing the pore loading, which may easily be done by varying the externally controlled process parameters, such as pressure or temperature [72]. Secondly, these studies may yield the complementary information on the pore space organization in porous solids with complexly organized pore spaces [80 - 83]. Figure 3.52 shows the effective diffusivities for cyclohexane in the nanoporous glasses.

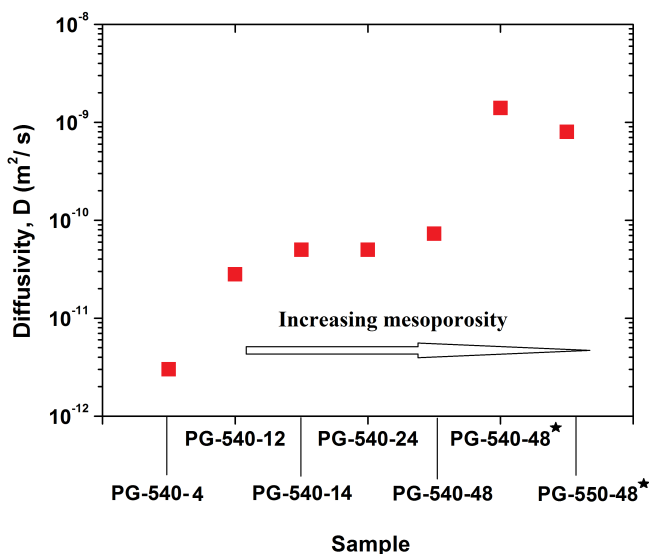


FIGURE 3.53: Effective diffusivities measured for different NPG samples at full pore loadings by cyclohexane.

The data of Figure 3.53 reveal that, among the family of the samples studied, there exist three distinct types of materials with notably differing diffusivities. The slowest diffusivity is found for the sample PG-540-4 prepared using the shortest heat treatment time and containing only small mesopores in the range between 2 to 4 nm. The molecules in this porous glass are therefore subject to very strong confinement effects, determining a dramatic decrease of the effective diffusivity beyond $D_0 = 1.4 \times 10^{-9} m^2 s^{-1}$ for bulk cyclohexane. Further contributions to the slowing down of the diffusivity come from (i) the existence of a large amount of necks, giving rise to restricted diffusion for molecules entrapped in the regions surrounded by the necks [84], and (ii) the surface interaction of the guest molecules with the pore. The enlargement of the pore sizes, including both of the necks and of the larger pores, which is achieved by increasing the treatment time beyond 4 h, gives rise to a considerable, more than tenfold increase of the diffusivities as compared to the sample PG-540-4. Only a slight effect of the treatment time in the range between 12 to 48 h was, however, observed. One may speculate that, for the given family of the samples, the major effect upon the diffusive transport comes from the pore space morphology, which turn out to be identical, but not the confinement effect or the surface interaction. Finally, the alkaline treatment leads to a dramatic improvement of the transport properties. It appears that the pore sizes in the alkaline-treated materials become sufficiently large to alter the diffusion properties and the porosity becomes sufficiently high to lead to the very tortuous pathways. We anticipate that the transport improvement is due to

the removal of the remaining colloidal deposits in the mesopore space during the alkaline treatment.

In the previous section, the situations of full loadings of the pore spaces by liquid phase were considered. But what may happen with variation of the pore loading? As one expect, it may complicate the diffusion behavior. Thus, if the gas density is very low, the gas-filled domains may be considered as impermeable obstacles, which may reduce the effective diffusivities [85]. If, however, the probe liquid possesses a sufficiently high pressure of its saturated vapor, the molecular flights through the gaseous phase may notably contribute to the overall mass transfer. It has recently been shown that [], for mesoporous solids, a moderate enhancement of the effective diffusivities can be expected on the basis of the fast-exchange equation:

$$D_{eff} = p_g D_g + p_s D_s \quad (3.12)$$

governing the mass transfer under these conditions. In Eq. (3.12), p_g and p_a ($p_g + p_a = 1$, $p_a = 1$) are the relative fractions of the molecules in the adsorbed and gaseous phases respectively, and D_g and D_a are the respective effective diffusivities in these two phases. As shown in Figure 3.53, this is exactly the case for cyclohexane used in the present study as a probe liquid. Indeed, we found that the diffusivities of the cyclohexane in the mesopores first increase with decreasing pore loading θ . At loadings below 0.2 the diffusivities, however, start to decrease with further decreasing pore loading. This behavior may easily be rationalized on the basis of Eq. (3.12) noting that p_g also changes with the changing of the pore loading. Indeed, it can be shown that p_g is directly proportional to the gas density and to the volume, available for the gaseous phase. At high θ , the effect of increasing volume available for the gaseous phase prevails over decreasing gas density (note that the relative amount adsorbed θ is interrelated with the gas pressure P and, therefore, the gas density via the adsorption isotherm). At low θ , in the region of one- or sub-monolayer coverage, the volume change available for the gaseous phase is negligible. The decrease of the gas density with decreasing θ results in the respective decrease of the effective diffusivities according to Eq. (3.12).

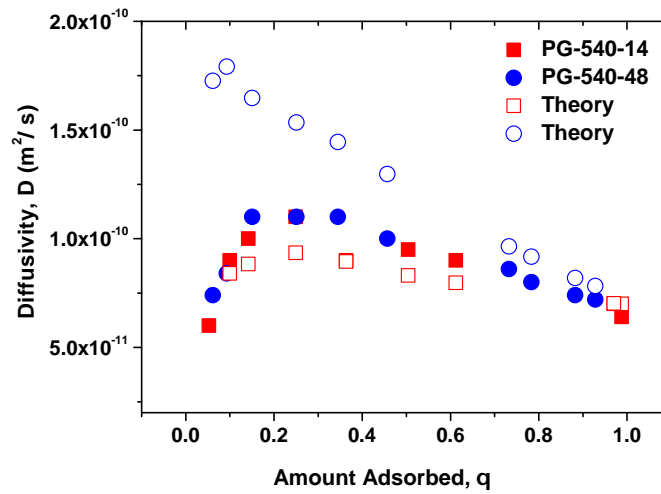


FIGURE 3.54: Effective diffusivities of cyclohexane in NPGs as a function of the relative pore loading.

All these effects discussed can easily be quantified. In particular, it has been shown that, assuming cylindrical pore geometry, D_{eff} , as given by Eq. (3.12), can be expressed as a function of the amount adsorbed θ :

$$D_{eff} = D_s + \frac{1 - \theta}{\theta} \frac{z(\theta) P_s M}{\rho_s R T} \left(\frac{d}{3} \sqrt{\frac{8RT(1 - \theta)}{\pi M}} - D_s \right) \quad (3.13)$$

where P is the gas pressure at loading θ and ρ_a is the density of the adsorbed liquid. By approximating the diffusivity in the gaseous phase by the Knudsen diffusivity:

$$D_K = \frac{d}{3} \sqrt{\frac{8RT}{\pi M}} \quad (3.14)$$

where v is the thermal velocity and d is the average pore size, the calculated diffusivities are found to be in a reasonable agreement (as it revealed by Figure 3.54) with the experimental data of Figure 3.53. Small discrepancies (by factors less than 2) may be associated with the fact that the classical Knudsen diffusivity, as given by Eq. (3.14), has been used in the calculations. It is, however, known that the numerical factor in this equation can depend on the geometry of the pore space [86].

3.4.5 Conclusions

In this section, we presented the results of a combined gas adsorption, NMR cryoporometry and pulsed field gradient NMR diffusometry study of structural and transport properties of a family of nanoporous glasses obtained by leaching of phase-separated borosilicate glasses. Different samples obtained by an intentional variation of the heat treatment times, during which the process of macrophase separation determining the resulting pore structure has occurred, were investigated.

One of the particular goals was to follow the structural evolution of the thus obtained porous glasses with increasing heat treatment time. Based on the nitrogen adsorption and NMR cryoporometry data, it has been concluded that after a short treatment of a few hours only a continuous network of small mesopores with the pore sizes between 2 – 4 nm was formed. Further treatment up to 24 h led to the enlargement of the majority of the mesopores, which were found to be in the range of about 6 – 7 nm. At the same time, only a very small increase of the size of the smallest pores to about 3 nm was noticed. Notably, this size of the smallest mesopores remained almost independent of the treatment duration, but the density of such mesopores decreased continuously. It is anticipated that the occurrence of these small mesopores does not result from the peculiarities of the phase separation process, but is caused by the remaining byproducts developed during the leaching process. With the treatment times above 48 h, a continuous mesopore network consisting of only relatively large mesopores above 5 nm was achieved. The obtained structural information is found to be in a good correlation with their transport properties. Thus, for the porous glass containing solely small mesopores (4 h treatment time), the diffusivities of the capillary-condensed cyclohexane were found to be about two orders of magnitude slower than the bulk diffusivity. This is attributed to a combined effect of the pore morphology, confinement effect, and interaction of the guest molecules with the inner surface of the porous glasses. For the porous glasses obtained with heat the treatment times up to 24 h, in which the notably larger pores were found to be separated by sufficiently smaller ones, a considerable improvement of the transport properties was experimentally proved.

Based on the data obtained, it was anticipated that the pore morphology has the major effect upon the long-range diffusivities measured. The options to improve the transport were demonstrated using the procedure of alkaline treatment and by decreasing the pore loading. In the latter case, the mass transfer via the gas phase was shown to lead to the diffusivity enhancement at the intermediate pore loadings, but to the diffusivity impairment at the low ones. The structural and

transport information obtained in this work for porous glasses prepared via the process of phase separation of borosilicate glasses and their correlations with the preparation conditions may be used for rational design of host-guest systems for practical applications.

Chapter 4

Summary

In our work, the advantages of PFG NMR were utilized to study the structure-dynamics relationships in several complex systems:

1) The aqueous solutions of dextran with different molecular weights from 10 kDa to a few hundreds kDa have proven to be a good model system to reproduce the situation of the so-called molecular crowding in biological cells. In such systems, which were mostly studied by fluorescence correlation spectroscopy (FCS), deviations from normal diffusion, namely anomalous subdiffusion have earlier been observed. The fundamental mechanisms governing such anomalous behavior, however, remained essentially unrevealed. By performing ensemble-based diffusion NMR studies in the same systems, we have complemented the earlier obtained data on anomalous diffusion and have shown the transition to normal diffusion on a larger time scale. We succeeded in reducing the gap between both techniques, leaving a sufficiently narrow range of the diffusion paths lengths, where the transition from anomalous (at shorter length scales) to normal diffusion (at longer ones) occurs.

2) Microemulsions have shown a number of remarkable properties, which often originate from a spatial anisotropy existing in such systems. The assessment of these properties is a challenging experimental problem. In this work, we report on the PFG NMR study of nematic microemulsions consisting of nano-sized micelles dissolved in a liquid crystal (5CB). It has earlier been shown that these nematic microemulsions may possess a local order, i.e., undergo a transition to nematic phase on a length scale on the order of micellar size, but remain isotropic on a longer scale within a narrow temperature range. Moreover, it was found that upon the isotropic-nematic transition the system macroscopically separates into two phases,

liquid crystal and micelle-rich ones. However, the mechanisms of such phase behavior and its physical nature remained unresolved. Since these microemulsions are highly dynamic, PFG NMR was applied to gain a further insight into structure by probing molecular diffusivities. To the best of our knowledge, we have performed the first direct diffusion measurements of all system components and have found no peculiarities in the transport behavior during different phase transitions. One of important findings was the observation that the presence of water (no matter deuterated or normal) was decisive on occurrence of the macroscopic phase separation.

3) The third part of this thesis addresses heterogeneous effects in diffusion for fluids in porous solids, as probed using a combination of NMR cryodiffusometry and adsorption methods. Ionic liquids (ILs), salts with melting temperature below 100°C , under confinement may exhibit altered properties as compared to bulk. This includes, in particular, shifted melting temperatures. Using porous glasses with different pore sizes as a medium for confinement and a few selected ionic liquids, we studied the relationships between their phase state and dynamics and the confinement size. A detailed characterization of the porous glasses has been performed by using NMR cryoporometry and nitrogen gas adsorption. Besides the absence of a sharp melting transition, both in pores and in bulk, the ILs used revealed very large temperature shifts in the pores. The melting temperature suppressions were found to exceed those obtained for most organic liquids. Diffusion studies complemented the data about the complex character of melting of the ionic liquids. Unexpectedly, the diffusion in pores was found to be faster than in bulk within a broad temperature range. The mechanism governing this behavior was proposed. In addition, we have performed correlations of the observed characteristics of the ionic liquids with their internal chemical structure, namely with the aliphatic chain lengths and the number of functional groups (CH₃) in cations.

4) Finally, a series of nanoporous glasses obtained by leaching of phase-separated alkali borosilicate glasses was investigated. These glasses have attracted a lot of attention in the field of catalysis, mass separation, drug delivery, etc. Changing only a few preparation parameters, such as temperature and treatment time, one can tune the pore structure characteristics of the porous glasses. The goal of this study was to correlate the preparation conditions of the porous glasses with the resulting structural and transport properties. We have shown that the combination of gas adsorption, NMR cryoporometry and pulsed field gradient NMR diffusometry yields a comprehensive set of information on both structure and transport properties. The pore size distributions and the pore interconnectivity were quantified.

Diffusion studies have shown nice correlations between structural and transport characteristics of the glasses. Thus, increasing mesoporosity and the pore network organization, which are functions of the heat treatment time, resulted in a non-monotonic variation of diffusivities.

Bibliography

- [1] A. Fick, "Über Diffusion", *Annalen der Physik*, vol. 94, pp. 59-86, 1855.
- [2] J. Kärger and R. Valiullin, "Mass Transfer in Mesoporous Materials: The Benefit of Microscopic Diffusion Measurement", *Chem. Soc. Rev.*, vol 42 (9), pp. 4172, 2013.
- [3] P.J. Langley and J. Hulliger, "Nanoporous and mesoporous organic structures: new openings for materials research", vol. 28 (5), pp. 279-291, 1999.
- [4] D. Enke, F. Friedel, F. Janowski et al., "In characterization of Porous Solids VI", Elsevier Science, Amsterdam, 2002.
- [5] M.J. Earle, K.R. Seddon, "Ionic liquids. Green solvents for the future", *Pure and Applied Chemistry*, vol. 72 (7), pp. 1391-1398, 2000.
- [6] M. Armand, F. Endres, D. MacFarlane et al., "Ionic-liquid materials for the electrochemical challenges of the future", *Nature Materials*, vol. 8 (8), pp. 621-629, 2009.
- [7] P.S. Schulz, "Ionic Liquids as Solvent Probes for NMR Cryoporometry", *ChemPhysChem*, vol. 11 (1), pp. 87-89, 2010.
- [8] M. Weiss, M. Elsner et al., "Anomalous Subdiffusion Is a Measure for Cytoplasmic Crowding in Living Cells", *Biophysical Journal*, vol. 87 (5), pp. 3518 - 3524, 2004.
- [9] M.J. Saxton, "Wanted: A Positive Control for Anomalous Subdiffusion", *Biophysical journal*, vol. 103 (12), pp. 2411-2422. 2012.
- [10] J. Yamamoto and H. Tanaka, "Transparent nematic phase in a liquid-crystal-based microemulsion", *Nature*, vol. 408 (6818), pp. 321-325, 2000.

- [11] A. Lebar, H. Tanaka et al., "Phase separation in nematic microemulsions probed by one-dimensional spectroscopic deuteron magnetic resonance microimaging", *Physical Review E*, vol. 78 (3), 2008.
- [12] Z. Chen and R. Nozaki, "Time-dependent phase behavior of 5CB-DDAB-water microemulsions monitored by means of dielectric spectroscopy", *Physical Review E*, vol. 84(1), pp. 011401, 2011.
- [13] G. Toquer et al., "Lyotropic Structures in a Thermotropic Liquid Crystal", *Langmuir*, vol. 23 (7), pp. 4081-4087, 2007.
- [14] F. Stallmach, "Fundamentals of Pulsed Field Gradient Nuclear Magnetic Resonance", script of lectures, 2004.
- [15] R.M. Cotts, M.J.R. Hoch, T. Sun et al., "Pulsed field gradient stimulated echo methods for improved NMR diffusion measurements in heterogeneous systems", *Journal of Magnetic Resonance*, vol. 83 (2), pp. 252-266, 1989.
- [16] R. Valiullin, P. Kortunov, J. Kärger, et al., "Concentration-dependent self-diffusion of liquids in nanopores: A nuclear magnetic resonance study", *Journal of Chemical Physics*, vol. 120 (24), pp. 11804-11814, 2004.
- [17] R. Valiullin, J. Kärger, R. Gläeser, "Correlating phase behaviour and diffusion in mesopores: perspectives revealed by pulsed field gradient NMR", *Physical Chemistry Chemical Physics*, vol. 11 (16), pp. 2833-2853, 2009.
- [18] J.H. Strange, M. Rahman, E.G. Smith, "Characterization of Porous Solids by NMR", *Phys. Rev. Lett.*, vol. 71 (21), pp. 3589-3591, 1993.
- [19] J. Mitchell, J. Webber, W. Beau, J. H. Strange, "Nuclear magnetic resonance cryoporometry", *Physics Reports*, vol. 461 (1), pp. 1-36, 2008.
- [20] O. Petrov, I. Furo, "NMR cryoporometry: Principles, applications and potential", *Progress in Nuclear Magnetic Resonance Spectroscopy*, vol. 54 (2), pp. 97-122, 2009.
- [21] D. Kondrashova, C. Reichenbach, and R. Valiullin, "Probing pore connectivity in random porous materials by scanning freezing and melting experiments", *Langmuir*, vol. 26 (9), pp. 6380-6385, 2010.
- [22] D. Kondrashova and R. Valiullin, "Improving structural analysis of disordered mesoporous materials using NMR cryoporometry", *Microporous and Mesoporous Materials*, vol. 178, pp. 15-19, 2013.

- [23] I. Hitchcock et al., "Studies of freezing-melting hysteresis in cryoporometry scanning loop experiments using NMR diffusometry and relaxometry", *Chemical Engineering Science*, vol. 66(4), pp. 582-592, 2011.
- [24] A.S. Verkman, "Solute and Macromolecule Diffusion in Cellular Aqueous Compartments", *Trends in Biochemical Sciences*, vol. 27 (1), pp. 27-33, 2002.
- [25] A.P. Minton, "The influence of macromolecular crowding and macromolecular confinement on biochemical reactions in physiological media", *Journal of biological chemistry*, vol. 276 (14), pp. 10577-10580, 2001.
- [26] R.J. Ellis, "Macromolecular crowding: obvious but underappreciated", *Trends in Biochemical Sciences*, vol.26 (10), pp. 597-604, 2001.
- [27] T.J. Feder et al., "Constrained diffusion or immobile fraction on cell surfaces: A new interpretation", *Biophysical journal*, vol. 70 (6), pp. 2767-2773, 1996.
- [28] M.J. Saxton and K. Jacobson, "Single-particle tracking: Applications to membrane dynamics", *Annual review of Biophysics and Biomolecular structure*, vol. 26, pp. 373-399, 1997.
- [29] M. Weiss et al., "Anomalous Subdiffusion Is a Measure for Cytoplasmic Crowding in Living Cells", *Biophysical Journal*, vol. 87 (5), pp. 3518 - 3524, 2004.
- [30] D.S. Banks, C. Fradin, "Anomalous diffusion of proteins due to molecular crowding", *Biophysical Journal*, vol. 89 (5), pp. 2960-2971, 2005.
- [31] K. Ritchie, X.Y. Shan, J. Kondo et al., "Detection of non-Brownian diffusion in the cell membrane in single molecule tracking", *Biophysical Journal*, vol. 88 (3), pp. 2266-2277, 2005.
- [32] A. Lubelski, J. Klafter, "Temporal correlation functions of concentration fluctuations: An anomalous case", *Journal of physical chemistry*, vol. 112 (40), pp. 12740-12747, 2008.
- [33] J. Szymanski, M. Weiss, "Elucidating the Origin of Anomalous Diffusion in Crowded Fluids", *Physical Review Letters*, vol. 103 (3), Article Number: 038102, 2009.
- [34] J. Wu, K.M. Berland, "Propagators and time-dependent diffusion coefficients for anomalous diffusion", *Biophysical Journal*, vol. 95 (4), pp. 2049-2052, 2008.

- [35] Y. He, S. Burov, R. Metzler et al., "Random time-scale invariant diffusion and transport coefficients", *Physical Review Letters*, vol. 101 (5), 2008.
- [36] I. Golding, E.C. Cox, "Physical nature of bacterial cytoplasm", *Physical Review Letters*, vol. 96 (9), Article Number: 098102, 2006.
- [37] N. Fakhri, F.C. MacKintosh, B. Lounis, "Brownian Motion of Stiff Filaments in a Crowded Environment", *Science*, vol. 330 (6012), pp. 1804-1807, 2010.
- [38] J-H. Jeon, V. Tejedor, S. Burov et al., "In Vivo Anomalous Diffusion and Weak Ergodicity Breaking of Lipid Granules", *Physical Review Letters*, vol. 106 (4), Article Number: 048103, 2011.
- [39] M.J. Saxton, "Anomalous subdiffusion in fluorescence photobleaching recovery: A Monte Carlo study", *Biophysical Journal*, vol. 81 (4), pp. 2226-2240, 2001.
- [40] J. Ries and P Schuille, "Fluorescence Correlation Spectroscopy", *BioEssays*, vol. 34, pp. 361-368, 2012.
- [41] M. Magdziarz, A. Weron, K. Burnecki, et al., "Fractional Brownian Motion Versus the Continuous-Time Random Walk: A Simple Test for Subdiffusive Dynamics", *Physical Review Letters*, vol. 103 (18), Article Number: 180602, 2009.
- [42] S.C. Weber, A.J. Spakowitz, J.A. Theriot, "Bacterial Chromosomal Loci Move Subdiffusively through a Viscoelastic Cytoplasm", *Physical Review Letters*, vol. 104 (23), Article Number: 238102, 2010.
- [43] A. Lubelski, I.M. Sokolov, J. Klafter, "Nonergodicity mimics inhomogeneity in single particle tracking", *Physical Review Letters*, vol. 103 (18), Article Number: 250602, 2008.
- [44] D. Ernst, M. Hellmann, J. Kohler, M. Weiss, "Fractional Brownian motion in crowded fluids", *Soft Matter*, vol. 8 (18), pp. 4886-4889, 2012.
- [45] M. Hellmann, J. Klafter, W. Dieter et al., "Challenges in determining anomalous diffusion in crowded fluids", *Journal of Physics-Condensed Matter*, vol. 23, Article Number: 234113, 2011.
- [46] P.T. Callaghan, "Principles of Nuclear Magnetic Resonance Microscopy", Clarendon Press: Oxford, U.K., 1991.
- [47] W.S. Price, "NMR Studies of Translational Motion", University Press: Cambridge, U.K., 2009.

- [48] B. Hakansson, M. Nyden, O. Soderman "The influence of polymer molecular-weight distributions on pulsed field gradient nuclear magnetic resonance self-diffusion experiments", *Colloid and Polymer Science*, vol. 278 (5), pp. 399-405, 2000.
- [49] M.C. Miller, A. Klyosov, D. Platt et al., "Using pulse field gradient NMR diffusion measurements to define molecular size distributions in glycan preparations", *Carbohydrate research*, vol. 344 (10), pp. 1205-1212, 2009.
- [50] H. Walderhaug, O. Soderman, D. Topgaard, "Self-diffusion in polymer systems studied by magnetic field-gradient spin-echo NMR methods", *Progress in Nuclear Magnetic Resonance Spectroscopy*, vol. 56 (4), pp. 406-425, 2010.
- [51] A. I. Maklakov, V. D. Skirda, N. F. Fatkullin, "Self-Diffusion in Polymer Systems", In *Encyclopedia of Fluid Mechanics*, Chremisinoff, N. M., Ed.; Gulf Publishing Co.: Houston, TX, vol. 9, 1990.
- [52] G. M. König et al., "Single nanoparticle tracking reveals influence of chemical functionality of nanoparticles on local ordering of liquid crystals and nanoparticle diffusion coefficients", *Nano Letters*, vol. 7 (5307), pp. 2794-2801, 2009.
- [53] P. Poulin et al., "Novel colloidal interactions in anisotropic fluids", *Science*, vol. 275 (5307), pp. 1770-1773, 1997.
- [54] T. Turiv et al., "Effect of collective molecular reorientations on brownian motion of colloids in nematic liquid crystal", *Science*, vol. 362(6164), 2013.
- [55] H. Löwen, "Anisotropic self-diffusion in colloidal nematic phases", *Physical Review E*, vol. 59 (2), pp. 1989-1995, 1999.
- [56] C.P. Lapointe, K. Mayoral and T.G. Mason, "Star colloids in nematic liquid crystals", *Soft matter*, vol. 9 (32), pp. 7843-7854, 2013.
- [57] U. Tkalec and I. Musevic, "Topology of nematic liquid crystal colloids confined to two dimensions", vol. 9 (34), pp. 8140-8150, 2013.
- [58] Z. Chen and R. Nozaki, "Does transparent nematic phase exist in 5CB/DDAB/water microemulsions? From the viewpoint of temperature dependent dielectric spectroscopy", *The Journal of Chemical Physics*, vol. 134(3), pp. 034505, 2011.
- [59] T. Bellini, M. Caggioni et al., "Fluctuation mediated interaction and phase separation of nanoparticles in a liquid crystal solvent", *Physical Review Letters*, vol. 91 (8), 2003.

- [60] P. Poulin, H. Stark, T. Lubensky and D.A. Weitz, "Novel Colloidal Interactions in Anisotropic Fluids", *Science*, vol. 275 (5307), pp. 1770-1773, 1997.
- [61] P.T. Callaghan, "Translational Dynamics and Magnetic Resonance", New York: Oxford University Press", 2011.
- [62] J.R. Sangoro et al., "Diffusion in ionic liquids: the interplay between molecular structure and dynamics", *Soft Matter*, vol. 7(5), pp. 1678-1681, 2011.
- [63] R. Kimmich, "NMR: tomography, diffusometry, relaxometry", Berlin Heidelberg: Springer-Verlag, 1997.
- [64] S.V. Dvinskikh and I. Furo, "Anisotropic self-diffusion in the nematic phase of a thermotropic liquid crystal by H-1-spin-echo nuclear magnetic resonance", *Journal of Chemical Physics*, vol. 115(4), pp. 1946-1950, 2001.
- [65] I. Furo and S.V. Dvinskikh, "NMR methods applied to anisotropic diffusion", *Magnetic Resonance in Chemistry*, vol. 40, pp. S3-S14. 2002.
- [66] E.E. Romanova et al., "Diffusion studies in confined nematic liquid crystals by MAS PFG NMR", *Journal of Magnetic Resonance*, vol. 196(2), pp. 110-114, 2009.
- [67] T. Welton, "Room-temperature ionic liquids. Solvents for synthesis and catalysis", *Chemical Reviews*, vol. 99(8), pp. 2071-2083, 1999.
- [68] A. Lewandovski and A. Swiderska "New composite solid electrolytes based on a polymer and ionic liquids", vol. 169 (1-4), pp. 21-24, 2004.
- [69] A. Menjoge et al., "Influence of Water on Diffusion in Imidazolium-Based Ionic Liquids: A Pulsed Field Gradient NMR study", *J. Phys. Chem.*, vol. 113, pp. 6353-6359, 2009.
- [70] C. Iacob et al., "Charge transport and diffusion of ionic liquids in nanoporous silica membranes", *Physical Chemistry Chemical Physics*, vol.12 (41), pp. 13798-13803, 2010.
- [71] U. Ciesla and F. Schütz, "Ordered mesoporous materials", *Microporous Mesoporous Materials*, vol. 27 (2-3), pp. 131-149, 1999.
- [72] D. Enke, F. Janowski, W.Schwieger, "Porous glasses in the 21st century—a short review", *Microporous Mesoporous Materials*, vol. 60 (1-3), pp. 19-30, 2003.

- [73] M. Thommes, B. Smarsly, M. Groenewolt et al., "Adsorption hysteresis of nitrogen and argon in pore networks and characterization of novel micro- and mesoporous silicas", *Langmuir*, vol. 22 (2), pp. 756-764, 2006.
- [74] D. Wallacher, K. Knorr, "Melting and freezing of Ar in nanopores", *Physical Review B*, vol. 63 (10), Article Number: 104202, 2001.
- [75] G. H. Findenegg, S. Jähnert, D. Akcakayiran, A. Schreiber, "Freezing and Melting of Water Confined in Silica Nanopores", *ChemPhysChem*, vol. 9 (18), pp. 2651 – 2659, 2008.
- [76] R. Schmidt, E.W. Hansen, M. Stockner, et al., "Pore-size determination of MCM-41 mesoporous materials by means of H-1-NMR Spectroscopy, N-2 adsorption, and HREM - A preliminary study", *Journal of American Chemical Society*, vol. 117 (4), pp. 4049-4056, 1995.
- [77] J. Kärger, D. M. Ruthven, D. Theodorou, "Diffusion in zeolites and other nanoporous materials", Wiley-VCH, Weinheim, 2012.
- [78] J. Kärger, C. Chmelik, R. Valiullin, *Phys. J.*, vol. 12 (4), pp. 39 – 45, 2013.
- [79] J. Kärger and R. Valiullin, "Mass Transfer in Mesoporous Materials: The Benefit of Microscopic Diffusion Measurement", *Chem. Soc. Rev.*, vol. 42, pp. 4172-4197, 2013.
- [80] J. Kärger and R. Valiullin, "The impact of mesopores on mass transfer in nanoporous materials: evidence of diffusion measurement by NMR", *Chemie Ingenieur Technik*, vol. 83, pp. 166-176, 2011.
- [81] T. Kirchner, A. Shakhov, P. Zeigermann, R. Valiullin, J. Kärger, "Probing Mesopore Connectivity in Hierarchical Nanoporous Materials", *Carbon*, vol. 50 (13), pp. 4804 – 4808, 2012.
- [82] D. Mehlhorn, R. Valiullin, J. Kärger, K. Cho, and R. Ryoo, "Exploring Mass Transfer in Mesoporous Zeolites by NMR Diffusometry", *Materials*, vol. 5, 699, 2012.
- [83] P. Zeigermann, J. Kärger and R. Valiullin, "Diffusion in Microporous Materials with Embedded Mesoporosities", *Microporous Mesoporous Materials*, vol. 178, pp. 84-89, 2013.
- [84] R. Valiullin and V. Skirda, "Time dependent self-diffusion coefficient of molecules in porous media", *Journal of Chemical Physics*, vol. 114, pp. 452, 2001.

[85] D. Mehlhorn, R. Valiullin, J. Kärger, K. Cho, and R. Ryoo, "Intracrystalline Diffusion in Mesoporous Zeolites", *ChemPhysChem*, vol. 13 (6), pp. 1495-1499. 2012.

[86] P. Zeigermann, S. Naumov, S. Mascotto, J. Kärger, B.M. Smarsly, and R. Valiullin, "Diffusion in hierarchical mesoporous materials: Applicability and generalization of the fast-exchange diffusion model", *Langmuir*, vol. 28 (7), pp. pp 3621-3632, 2012.

Acknowledgements

First of all I want to express my sincere gratitude to my supervisor Dr. Rustem Valiullin. He taught me what the real science is, how to approach the boundless sea of knowledge, how to work hard but with interest and satisfaction. All these years I could immediately get help and thoughtful comments about my research. Besides I learned a lot not only about science but also about the personal attitude to life in general.

Professor Jörg Kärger causes admiration in every individual who knows him. He is so much devoted to the Science that every student in our institute might be jealous to his attitude and infinite energy.

I'm thankful about invaluable aid from my colleagues Philipp Zeigermann and Dirk Mehlhorn with experiments and multiple advises in theoretical field. Due to them my first steps in research had been implemented.

The functioning of my main working tool, NMR spectrometer, couldn't be possible without Stefan Schlayer, who wasn't showing any sign of discontent even when I did something wrong because of the lack of experience.

My colleagues from Department of Chemistry, Christian Reichenbach and professor Dirk Enke were the most reliable providers of samples, what resulted in very productive collaboration.

Lutz Moschkovitz has always been showing a lot of patience, preparing samples for me and trying to understand my poor german language.

D. Kondrashova, D. Schneider, A. Laurer, J. Chiprian, K. Wydcliffe, M. Drob, H. Gadaili and K. Skobeltsyn made up the really interesting and joyful company during my time here.

Special thanks to DFG, IRTG, the financial foundation is gratefully acknowledged. Thanks to the University for wise placing and bringing me into contact with students from Max Plank Institute and my current flatmates Lorenzo Taggi and Wiktor Mlynarski who became my best friends and from whom I've learned so much during our discussions.

Last but not least, I want to thank my family, for supporting me despite of the large distances.

List of Publications

Journal Publications

- A. Shakhov, R. Valiullin, and J. Kärger, Tracing Molecular Propagation in Dextran Solutions by Pulsed Field Gradient NMR, *J. Phys. Chem. Lett.*, 3 (2012) 1854.
- A. Shakhov, C. Reichenbach, D. Kondrashova, P. Zeigermann, D. Mehlhorn, D. Enke, and R. Valiullin, Exploring Internal Structure of Nanoporous Glasses Obtained by Leaching of Phase-Separated Alkali Borosilicate Glasses, *Chem. Ing. Tech.*, 85 (2013) 1734.
- T. Kirchner, A. Shakhov, P. Zeigermann, R. Valiullin, and J. Kärger, Probing Mesopore Connectivity in Hierarchical Nanoporous Materials, *Carbon*, 50 (2012) 4084.
- A. Shakhov, J. Kärger, and R. Valiullin, Diffusion Properties of Liquid-Crystal-Microemulsion Mixtures, *Colloid and Polymer Science*, submitted.
- A. Shakhov, K. Wycliffe, H. Gadaili and R. Valiullin, NMR cryoporometry based on ionic liquids, in preparation.

Oral Presentations

- A. Shakhov, Diffusion in crowded environments, 15th IRTG Workshop, Leipzig University, 04/2012.
- A. Shakhov, Diffusion in crowded environments (comparing FCS and NMR data), SFG meeting, Dresden, 09/ 2012.
- A. Shakhov, Probing mesopore connectivity in hierarchical porous materials, XVI. POROTEC Workshop, Bad Soden, Germany, 11/2012.

Poster Presentations

- A. Shakhov, J. Kärger, R. Valiullin, Tracing Molecular propagation in Dextran Solutions by Pulsed Field Gradient NMR, MRPM11 Conference, University of Surrey, Guildford, UK, 09/2012.
- A. Shakhov, C. Reichenbach, D. Enke and R. Valiullin, NMR characterization of nanoporous glasses, XVI. POROTEC Workshop, Bad Soden, Germany, 11/2012.
- A. Shakhov, C. Reichenbach, D. Enke and R. Valiullin, Structural and transport properties of nanoporous glasses with tuned micro- and mesoporosity, XXV Deutsche Zeolith Tagung, Hamburg, Germany, 03/2013.
- A. Shakhov, J. Kärger and R. Valiullin, Tracing Molecular propagation in Dextran Solutions by Pulsed Field Gradient NMR, Diffusion Fundamentals 5, Leipzig, Germany, 08/2013.

Curriculum Vitae

Personal data

Family name	Shakhov
First name	Alexander
Date of Birth	16.03.1986
Place of Birth	Kursk, UdSSR
Nationality	Russian
E-Mail	alexander.shakhov@uni-leipzig.de

Education

1993-2003	School, Fatezh(Kursk Oblast), Russia
2003-2009	Physics studies, MEPhI, Moscow, Russia
2009	Topic of diploma thesis: "Investigation of Carbon Nanotubes by Raman Spectroscopy"
Since 2011	Ph.D. student in Department of Interface Physics, Faculty of Physics and Earth Sciences, Leipzig University Associated member of the International Research Training Group "Diffusion in Porous Materials"

Declaration / Selbständigkeitserklärung

Hiermit erkläre ich, dass ich die vorliegende Arbeit selbständig und ohne unzulässige Hilfe oder Benutzung anderer als der angegebenen Hilfsmittel angefertigt habe. Ich versichere, dass Dritte von mir weder unmittelbar noch mittelbar geldwerte Leistungen für Arbeiten erhalten haben, die im Zusammenhang mit dem Inhalt der vorliegenden Dissertation stehen, und dass die vorliegende Arbeit weder in Inland noch im Ausland in gleicher oder ähnlicher Form einer anderen Prüfungsbehörde zum Zwecke einer Dissertation oder eines anderen Prüfungsverfahrens vorgelegt und in ihrer Gesamtheit noch nicht veröffentlicht wurde. Alles aus anderen Quellen oder von anderen Personen übernommene Material, das in der Arbeit verwendet wurde oder auf das direkt Bezug genommen wird, wurde als solches kenntlich gemacht. Insbesondere wurden alle Personen genannt, die direkt an der Entstehung der vorliegenden Arbeit beteiligt waren. Es haben keine erfolglosen Promotionsversuche stattgefunden.

Leipzig, den 09. Mai 2014

Alexander Shakhov

